The Astrophysical Journal, 604:906–923, 2004 April 1

PLASMA FLOWS OBSERVED IN MAGNETIC FLUX CONCENTRATIONS AND SUNSPOT FINE STRUCTURE USING ADAPTIVE OPTICS

Thomas R. Rimmele
National Solar Observatory,[1] Sunspot, NM 88349; rimmele@nso.edu
Received 2003 October 3; accepted 2003 December 16

ABSTRACT

We present diffraction-limited observations of magnetic flux concentrations and penumbral and umbral fine structure within an active region observed at disk center. We recorded G-band images, magnetograms, Dopplergrams, and narrowband filtergrams, using the Universal Birefringent Filter (UBF) at the Dunn Solar Telescope (DST). The National Solar Observatory (NSO) adaptive optics system at the DST was used to achieve diffraction-limited long-exposure imaging with a high signal-to-noise ratio. The main results can be summarized as follows: Strong and spatially narrow downflows are observed at the edge of magnetic structures, such as small flux concentrations (sometimes also referred to as flux tubes), pores, a light bridge, and the sunspot umbrae. For the particular sunspot observed, we find strong evidence for what appear to be vigorous, small-scale convection patterns in a light bridge. We observe extremely narrow ($<0\farcs2$) channels or sheets of downflowing plasma. Flux concentrations as seen in intensity expand from a height close to where the continuum is formed to the height of formation for the G band. These observations indicate that the G band forms in the mid-photosphere. We are able to identify individual penumbral fibrils in our data and find a bright (hot) upflow and a more vertical field structure at the filament footpoint near the umbral boundary. The observations are consistent with a filament geometry in which the field and flow turn to a nearly horizontal, dark structure over a distance of about $0\farcs2$. In the deep photosphere we observe strong upflows of the order of 1 km s^{-1} in umbral dots. We compare our results with theoretical model predictions.

Subject headings: instrumentation: adaptive optics — Sun: magnetic fields — sunspots

1. INTRODUCTION

Small-scale magnetic field concentrations are of fundamental importance to solar astronomy and astrophysics in general. Magnetic flux outside sunspots is often localized in small-scale, kilogauss-strength (kG) magnetic concentrations found predominately in intergranular lanes (Muller 1975; see the review by Muller 1994 and references therein). Magnetic flux concentrations are seen as bright points (BPs) when observed in the G-band and with sufficiently high spatial resolution (Title & Berger 1996; Muller et al. 2000; Berger & Title 2001). G-band BPs are therefore often used as a proxy to study the dynamics of magnetic flux concentrations (Berger et al. 1995, 1998; Berger & Title 1996; van Ballegooijen et al. 1998; Muller et al. 2000; Nisenson et al. 2003). The size of the flux elements (or G-band BPs) is of the order of 100 km or less and thus is at or below the diffraction limit of existing solar telescopes, which makes observations of these structures extremely challenging.

The exact physical mechanisms that make small magnetic flux concentrations appear bright in G-band filtergrams are not entirely understood (Rutten et al. 2001; Steiner, Hauschildt, & Bruls 2001), although significant progress has been made recently (Schüssler et al. 2003). The field strengths of the flux concentrations ranges from 1500 to 1700 G. See Solanki (1993) for a comprehensive summary of magnetic field strengths measurements of small-scale magnetic elements.

The interaction of magnetic fields and plasma flows is one of the fundamental astrophysical physical processes that leads to many of the dynamic effects observed on the Sun. Flux concentrations are constantly moved around by convective flows. As a consequence, field lines get twisted and tangled, which leads to energy buildup in magnetic structures. This excess energy can eventually be released in flares (e.g., Gerrard, Arber, & Hood 2002). The constant buffeting of flux concentrations by convective motions is expected to produce MHD waves that can travel along the field lines into the upper layers of the atmosphere. Dissipation of these waves may contribute to the heating of the upper atmosphere (e.g., Muller et al. 1994).

The interchange instability (Parker 1975; Piddington 1975; Steiner 1999) inherent to small flux concentrations is believed to be the cause for their short lifetime. Observations show that flux concentrations fragment or are shredded by convective motions on timescales of minutes (Berger & Title 1996). The small spatial scale and their dynamic behavior, but also their short lifetime, make, in particular, quantitative measurements of physical parameters of these structures, such as velocity and magnetic field, an extremely challenging task. In comparison, theoretical models and simulations have rapidly advanced over the last decade and are at a point where these models are able to guide observations with very detailed predictions (Steiner et al. 1998; Grossmann-Doerth, Schüssler, & Steiner 1998; Stein, Brandenburg, & Nordlund 1992; Stein, Bercik, & Nordlund 2003; Stein & Nordlund 1998; Bercik, Nordlund, & Stein 2003). See, for example, Schüssler (2001) for a review of the current state of the art of MHD models.

Simulated observables, such as the Stokes vector "measurements" in Fe i lines, including dynamical effects can be provided by these models (two- and three-dimensional) and are an indispensable tool to guide and interpret observations of flux concentrations (e.g., Fig. 12 of Stein et al. 2003). However, because of the lack of sufficient spatial resolution, it has been impossible to observationally verify even the

[1] NSO is operated by the Association of Universities for Research in Astronomy (AURA), Inc., under contract to the National Science Foundation.

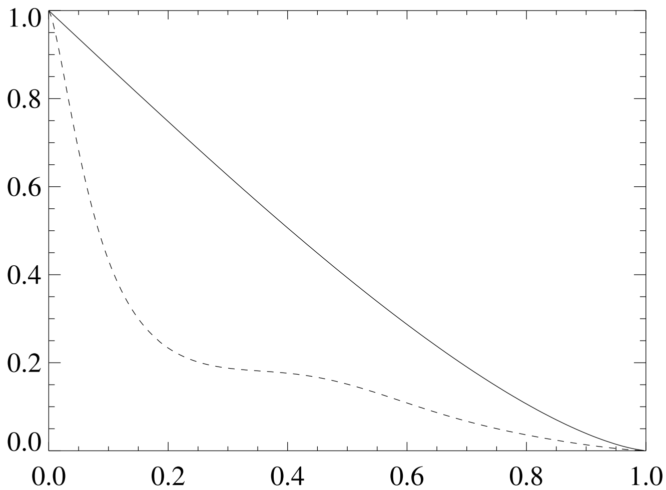

Fig. 1.—Estimated MTF for AO-corrected long-exposure images ($\lambda = 630$ nm) as a function of spatial frequency normalized to the diffraction limit λ/D. The theoretical telescope MTF of the DST is shown for comparison. Although the amplitudes are attenuated, the AO retains the high spatial frequency information in the images. The corresponding PSF is characterized by a diffraction-limited core on top of a seeing halo. The width of the seeing halo is determined by the size of the Fried parameter $r0$ and is of the order of $1''$.

most fundamental predictions of such models. For example, because of the steep decrease in gas pressure as a function of height in the photosphere, the magnetic field is expected to fan out, and the diameter of the flux concentration is expected to increase with altitude. While a flux concentration is forming, models predict strong downflows within the field concentration. The downflow eventually leads to the evacuation of the flux concentration and is initiated or driven by radiative cooling at the surface, combined with the fact that the magnetic field inhibits convective energy transport within the magnetic structure. The magnetic field strength increases during this process, often referred to as *convective collapse* (Parker 1978; Spruit 1979; Steiner 1994; Grossmann-Doerth et al. 1998), resulting in kG fields. Once a mature kG flux concentration is formed, we expect to measure essentially zero velocity within the flux concentration. However, at the edge of the flux concentration a thin sheet of downflowing plasma has been predicted in the models. This strong downflow is driven by radiative heat losses into the evacuated magnetic structure and subsequent cooling of the surrounding plasma.

Direct observations that would confirm these fundamental predictions are still mostly lacking. A number of indirect observations have been performed that use the Stokes V zero crossing and asymmetry as diagnostic tools to derive information about the flow field of the unresolved magnetic component within the resolution element. For example, measurements of velocities in network and plage magnetic elements using the position of the Stokes V zero crossing indicate that, on average, a downflow on the order of 1 km s^{-1} is observed in areas where small-scale magnetic elements are present (see Steiner 1999 for a summary discussion of Stokes V zero-crossing observations). Strong magnetic elements tend to show downflows of smaller amplitude when compared to the weaker magnetic elements (Sigwarth et al. 1999). The asymmetry between the red and blue lobes of the Stoke V spectrum contains information about the flow field in and around flux elements (see, e.g., Steiner 1999 and references therein; Grossmann-Doerth et al. 2000). A strong downflow at the edge of an expanding flux tube, which according to models is an expected feature of a mature strong-field element, produces a positive area asymmetry. Statistical analysis of synthetic profiles (Steiner et al. 1996; Sigwarth et al. 1999), as well as observed Stokes V profiles on average, indeed show a positive area asymmetry (e.g., Sigwarth et al. 1999; Leka & Steiner 2001; Sankarasubramanian & Rimmele 2002).

In this paper we present diffraction-limited observations of small flux concentrations. The observations were performed with the help of the low-order adaptive optics (AO) system available at the Dunn Solar Telescope (DST; Rimmele 2000). The AO system allows diffraction-limited, long-exposure imaging, which is essential for quantitative, high-resolution spectroscopy and polarimetry. We present velocity and line-of-sight (LOS) magnetic field measurements that allow us to test some of the fundamental model predictions discussed above. The first part of this paper focuses on the small flux concentrations with a size of the order of $0\overset{''}{.}2$ or less (depending on the wavelength of the observation). We present quantitative measurements of the flow field in and around these flux elements.

The second part of the paper extends the velocity and magnetic field measurements to larger structures, including a light bridge (LB) and micropores. Small-scale flux concentrations sometimes coalesce and form larger structures, such as micropores and pores. The small flux concentrations, often referred to as flux tubes, are therefore sometimes called the building blocks of solar magnetism. According to three-dimensional MHD simulations (e.g., Stein, Bercik, & Nordlund 2002) micropores are expected to form preferably at the vertex of several granules. A micropore forms at a location where a weak granule disappears and leaves a void that is then filled by the magnetic flux. Once a sufficient amount of flux has been accumulated, a dark structure appears. Contrary to the small flux concentrations, the $\tau = 1$ line cuts the larger micropore at a lower temperature compared to its surroundings, and therefore the structure appears dark in the continuum images. An interesting detail of this dynamic model is that during the initial stages of its formation, the darkest part of the micropore does not coincide with maximum of the magnetic flux. We present observational evidence that confirms this aspect of the MHD model.

In § 4.3, we point out a variety of small-scale features, such as narrow, strong downflows that are commonly seen at the interface between magnetic and nonmagnetic plasma, i.e., the magnetopause. The physical mechanism that drives these flows appear to be common to many different magnetic structures, including small flux concentrations, pores, sunspot umbrae, and LBs.

We also present observations of penumbral filaments at sun center, as well as velocity measurements in umbral dots, and discuss our observational results in the context of theoretical models.

2. OBSERVATIONS

The observations were performed on 2001 April 14, at the 0.76 m DST in Sunspot, New Mexico. We observed a small active region at almost exactly disk center ($\cos \Theta = 0.998$). The National Solar Observatory (NSO) solar AO system (Rimmele 2000) at the DST was operated and was feeding a partially seeing-corrected beam to a set of imaging CCD cameras. The main instrument used for these observations was the Universal Birefringent Filter (UBF). The UBF is a tunable Lyot filter with a passband that varies between 180 and 250 mÅ as a function of wavelength. The UBF was tuned into the red and blue wings of several spectral lines, namely,

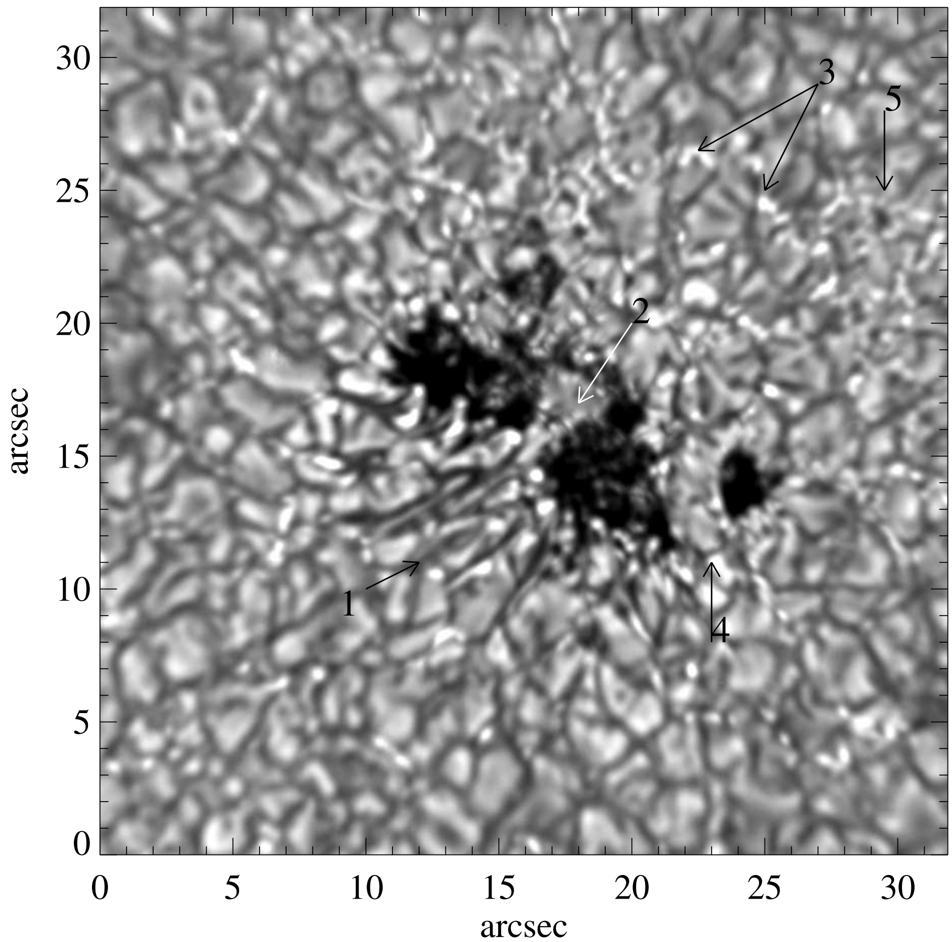

Fig. 2*a*

Fig. 2.—(*a*) The G-band image of the small active region observed at disk center. An effective 18 s exposure time was achieved by averaging a number of individual *UBF* filtergrams that were recorded with a 1.5 s exposure time. The fact that spatial structure at the diffraction limit is visible in these long-exposure data demonstrates the effectiveness of the AO correction. (*b*) Dopplergram of the same active region. Dark denotes downflows and bright upflows. (*c*) Magnetogram of active region. A correlation between magnetic field and G-band BPs is apparent. The arrows point to features discussed in detail in the text: (1) rudimentary penumbra; (2) field-free region, or LB, with strong, narrow downflows; (3) examples of BPs; (4) region of opposite polarity between umbral fragments; (5) micropore.

Fe I λ5576, Fe I λ6302, and C I λ5380. The carbon line C I λ5380, which forms deep in the photosphere at an altitude of approximately 40 km (Fleck 1991), and the iron line Fe I λ5576, which forms at an altitude of about 320 km (Bruls, Lites, & Murphy 1991), are used to obtain Dopplergrams at different heights in the solar atmosphere. The Fe I λ5576 line has the advantage of being a "nonmagnetic" line; i.e., the effective Landé factor is $g = 0$, providing a clean Doppler signal without any cross talk from the magnetic field. The carbon line has a g-factor of $g > 0$. However, because of the fairly broad bandpass of the UBF, the Dopplergrams measure a global line shift of the spectral lines, which are affected little by the Zeeman effect. The iron line Fe I λ6302 was used to obtain LOS magnetograms. A quarter-wave plate in front of the UBF enables us to record left- and right-circular polarization (LCP and RCP, respectively) filtergrams. The magnetograms were generated from the filtergrams taken in the blue wing of the Fe I λ6302 line, with an offset of 80 mÅ from line center. In addition to the blue-wing filtergrams, we recorded red-wing filtergrams with the same wavelength offset of 80 mÅ, in order to obtain simultaneous Dopplergrams along with the magnetograms.

In addition to the UBF data, we recorded G-band images, using a 1 nm wide interference filter centered at the CH-band head at 430.5 nm and broadband (10 nm) filtergrams at 500 nm. The UBF filtergrams were recorded with a 1K $\times$ 1K CCD camera with a pixel resolution of $0\farcs05$ pixel^{-1}. The G-band observations were done with a CCD with 1200×1200 pixels and a slightly higher pixel resolution of $0\farcs03$ pixel^{-1}. In both cases the images are oversampled. The diffraction limit, for example, at the G band is $0\farcs12$. The field of view (FOV) was approximately $50''$ for the UBF and $36''$ for the G-band camera. The exposure time was set to 1.5 s for all cameras.

We collected data over a period of about 45 minutes, from which the best images were selected for further processing and analysis, using image contrast as a selection criterion.

3. DATA REDUCTION

After flat and dark correction, the G-band images and UBF filtergrams were corrected for residual differential image motion visible across the extended FOV seeing effects by using a destretch algorithm. G-band images and UBF filtergrams were carefully aligned, which involved scaling up the UBF

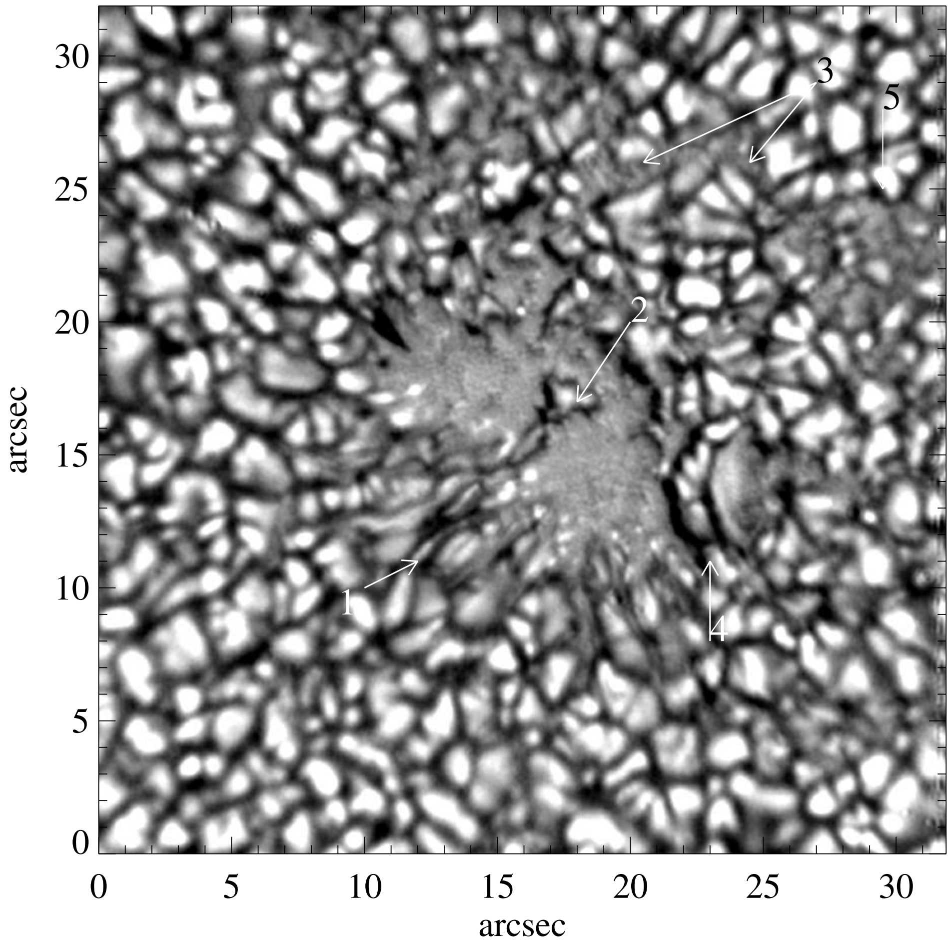

FIG. 2b

filtergrams to the higher 0.″03 pixel^{-1} resolution of the G-band images using a cubic spline interpolation. We computed Dopplergrams and magnetograms in the usual manner:

$$\text{Velocity} = c_v \frac{I_{\text{red}} - I_{\text{blue}}}{I_{\text{red}} + I_{\text{blue}}}, \tag{1}$$

$$B_{\text{LOS}} = c_B \frac{I_{\text{LCP}} - I_{\text{RCP}}}{I_{\text{LCP}} + I_{\text{RCP}}}. \tag{2}$$

The Dopplergrams were calibrated using a calibration factor (c_v) determined by modeling the spectral profile of the observed lines as observed through the UBF. The Liège atlas profile was convolved with the UBF passband, from which the calibration factor can be derived directly. The calibration factors were also verified experimentally for earlier observations by recording a spatially averaged spectral scan for each line. The calibration factors derived from the model and the experimental ones agree within a few percent (Hartkorn 2003). The zero point for the Dopplergrams was set by removing the mean of a quiet-Sun area from the Dopplergrams. The calibration factor for the magnetograms was derived in a fashion similar to what was described by Berger & Title (2001). The noise floor in the magnetograms was determined from the FWHM of a Gaussian fit to the histogram of the calibrated magnetogram (see Fig. 5 of Berger & Title 2001). The noise level for our long-exposure magnetograms is approximately 50 G, which is consistent with the number quoted by Berger & Title (2001) for their time-averaged (noise-reduced) magnetograms. However, the use of the AO system allows us to obtain these low noise levels while maintaining the diffraction-limited resolution.

In order to increase the signal-to-noise ratio (S/N), we averaged a number of UBF filtergrams before computing the Doppler- and magnetograms, respectively. This leads to a typical integration time for the averaged filtergrams of about 10 s. Compared to the timescale of the atmospheric seeing effects, these are truly long exposures. The AO system is essential for achieving diffraction-limited imaging, given these long integration times. However, as is true for any AO system, the NSO low-order AO system provides a partial correction of atmospheric seeing effects only. The degree of correction is usually specified by the Strehl ratio. The NSO low-order AO system has achieved Strehl ratios of $S > 0.5$ in good seeing conditions (Rimmele 2000).

We derived a rough estimate of the average long-exposure point-spread function (PSF), making the following assumptions. We assume that the Fried parameter is constant during the observing period. We measured the Fried parameter at the beginning and end of the observing run, using the AO systems wave front sensor in open loop, and used the average of $r_0 = 10.6$ cm to characterize the seeing conditions during the observations. In general, this is not necessarily a good assumption, since the seeing can vary significantly over the period of 45 minutes during which the data were obtained. Using integration times of 10 s will smooth out some of the

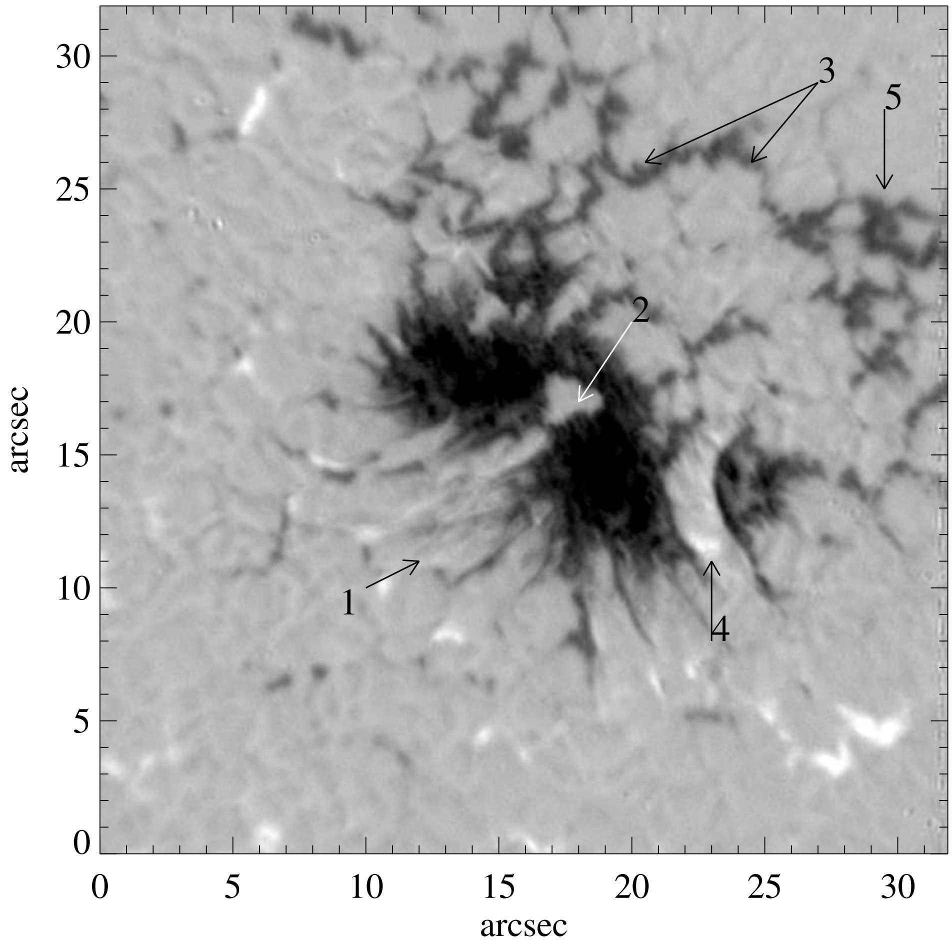

FIG. 2c

seeing variations. However, variations remain, are visible in the data, and will cause some of the images to be overcorrected, while others are undercorrected. We also do not take into account any aberrations present in the optical setup that are not corrected by the AO system, i.e., aberrations introduced by uncommon-path optics. These include the UBF itself and various reimaging optics. Any uncommon-path aberrations are not represented in our PSF estimate and are not corrected. We did not attempt to quantify the uncommon-path aberrations, but we expect the uncommon-path wave front errors to be somewhat larger in the UBF channel than in the G-band channel, since the UBF path has more optical elements. The NSO AO system corrects for 15 Zernike modes (Rimmele 2000). For the purpose of estimating the PSF, we assume that the first 15 modes are corrected perfectly. The error introduced in the PSF estimate from neglecting the residual wave front errors in the corrected modes is small compared to the error introduced by not simultaneously measuring the Fried parameter, i.e., the variance of the residual wave front error of the uncorrected modes.

The estimate for the long-exposure PSF is used to deconvolve G-band images and UBF filtergrams, taking into account the $\lambda^{6/5}$ wavelength dependence of r_0. A simple Wiener filter was used to deconvolve the images. The noise estimate needed for the Wiener filter was derived from the high-frequency tail of the image power spectra. Not taking into account the uncommon-path aberrations and residual wave front errors in the corrected modes results in an overestimation of the Strehl ratio and an undercorrection of the deconvolved images. Our model long-exposure PSF has a Strehl ratio of $S = 0.36$ at 630 nm, which compares reasonably well to the experimentally determined average Strehl ratios (Rimmele 2000). Figure 1 shows the estimated modulation transfer function (MTF) compared to the theoretical telescope MTF of the DST.

4. RESULTS

Figures 2*a*, 2*b*, and 2*c* show a processed G-band image and the corresponding magnetograms and Dopplergrams, respectively, of the observed active region. The effective integration time for these particular data was 30 s. Structures at scales very close to the diffraction limit of the DST ($0\overset{''}{.}18$ at 630 nm) are visible in these data, showing the effectiveness of the AO system. Close inspection of the G-band image reveals that the image contrast is reduced toward the edges of the FOV, i.e., several arcseconds away from the lock point of the AO near the center of the FOV. This is an expected effect caused by anisoplanatism of the wave front errors.

Before focusing on several interesting aspects that are studied in detail below, we point out the following general features of this active region and give some context information. The sunspot shows two fragments with what could be described as a rather large LB between them. Within the FOV and in the direct vicinity of the sunspot we found a large number of BPs, which we used to study properties of flux concentrations. The sunspot itself had a vast amount of fine structure including umbral dots, the LB and a rudimentary penumbra on one side of the spot.

The fact that the active region is located at disk center makes it an ideal target to study vertical velocity and magnetic field components. The NSO/Sacramento Peak Hilltop flare patrol film was used to determine the evolutionary history of this particular active region. The region was a young and evolving region that had emerged several days prior to our observations. The region could be observed on the flare patrol film for at least 3 days after our observations were taken. About 30 minutes before our observing run, a small flare occurred within the region.

On the left side of the spot both sunspot fragments show elongated, filamentary structures in the LOS magnetogram ($B_{\rm LOS}$), indicating more inclined field lines. We identify these filamentary structures as *rudimentary penumbrae*. A number of small-scale, mixed-polarity features are also seen in this area. An interesting feature in the Dopplergram are the very narrow and strong downflows observed at the edge of the sunspot. This is discussed in detail in § 4.3. Most of the BPs, i.e., flux concentrations, are arranged in a network located in the upper right corner of the FOV. The cell size of this network is of the order of $2''$–$3''$, i.e., the size of a few granules. Although individual flux tubes evolve on much faster timescales, this small-scale network persists over the entire observing period (45 minutes). This can be seen from Figure 3, which shows a time sequence of magnetograms and the corresponding intensity and Doppler images.

Another interesting feature worthy to be pointed out is the opposite-polarity flux located between one of the umbral fragments and what appears to be a large pore or an additional, smaller umbral fragment. A very sharp neutral line separates the positive and negative polarity. During the course of the observations, the opposite (positive) flux between the two dark spot fragments nearly disappears, most likely because of flux cancellation. During the same time, strong downflows develop at the edge of the dark features.

4.1. *Bright Points*

4.1.1. *Velocities of Bright Points*

The high-resolution, high-S/N data obtained with the help of AO allow us to study physical properties of BPs. We are able to perform direct measurements of velocities in BPs and their vicinity. For this purpose we zoom in on small areas containing a number of BPs. Figure 4 shows at a higher magnification two smaller FOVs of approximately $6'' \times 6''$ that are part of the above-mentioned network of BPs. Shown are the Fe I λ6302 intensity, G-band intensity, magnetogram, and Dopplergram. We note that G-band BPs are generally also seen as bright structures in the Fe I λ6302 intensity. In comparing the intensity and the magnetogram, it is obvious that most small-scale magnetic flux concentrations are readily associated with BPs. In the Dopplergram we plot contour lines outlining the magnetic field concentrations.

At the very edge of flux concentrations we find narrow downdrafts. An example is seen in Figure 5, where we plot a cross section through an individual flux concentration. Plotted are the line and G-band intensity (showing the significantly higher contrast of the BPs in the G band), the Stokes *V* signal, and the velocity. A narrow downdraft with an amplitude on the order of a few hundred meters per second is located at the very edge, off to one side of the flux concentration. The spatial extent of the downdraft is about $0\farcs2$, i.e., right at the diffraction limit of the telescope. This indicates that these downdrafts are likely to be even narrower. Using the Stokes *V* amplitude as a selection criterion, we selected magnetic flux concentrations within the "network" in order to perform a statistical analysis of the BP regions. Figure 6 shows scatter plots of the selected pixels. Fig. 6*a* plots the Fe I λ6302 line intensity versus the LOS (vertical) component of the magnetic field. We observe a slight and nearly linear increase in intensity as the LOS magnetic field increases. Above a certain Stokes *V* amplitude, the structures suddenly turn darker again and, on average, have an intensity below that of the average photosphere. This turnover is due to the formation of micropores, which is discussed in more detail in § 4.2.

The velocity versus $B_{\rm LOS}$ scatter plot (Fig. 6*b*) reveals that for low $B_{\rm LOS}$ values the velocities tend to be mostly negative (downflow). As $B_{\rm LOS}$ increases, the velocities turn from negative to values close to zero, following a nearly linear relationship. To understand this behavior, we have to recall that the size of the flux concentrations observed here is at or below the diffraction limit of the DST. Consequently, the telescope PSF leads to mixing of information from within the flux concentration and its surroundings. Residual energy in the seeing halo that is not corrected for by the combined application of the AO and post facto reconstruction techniques will further contribute to this mixing. This effect will be most visible at the edge of the small flux concentrations, where $B_{\rm LOS}$ is weak. Since flux concentrations are predominately located in intergranular lanes, low $B_{\rm LOS}$ values tend to be associated with downflows that occur outside, but not inside, the magnetic feature. The fact that as we move closer to the center of the flux concentration (larger $B_{\rm LOS}$) the velocity gradually but steadily moves toward zero indicates that within the flux concentration the plasma tends to be at rest. We also note that for larger $B_{\rm LOS}$, the correlation between velocity and LOS magnetic field is much tighter, again indicating that mixing between different features of different physical properties due to the PSF is less of an issue here.

Figure 7 plots velocity versus intensity. The pixels were separated into two bins using the value of $B_{\rm LOS}$ as a criterion. One bin contains pixels that fall in the range 300 G $<$ $B_{\rm LOS} <$ 500 G, i.e., pixels that for the most part represent the interior of flux concentrations, but excludes pixels that represent micropores. The second bin contains the low-flux pixels ($B_{\rm LOS} <$ 200 G), which represent the edges of flux concentrations. It is obvious from Figure 7 that the two distributions are different. While the slope for the low-$B_{\rm LOS}$ distribution is very similar to that of the quiet-Sun distribution, the high-$B_{\rm LOS}$ pixels (the BP interiors) generally show very small velocities. The brightest features have velocities close to zero; i.e., the plasma is at rest in the center of the brightest flux concentrations. This again indicates that the low-$B_{\rm LOS}$ points at the edge of flux concentrations are contaminated by their immediate quiet-Sun surroundings.

We use the Dopplergrams taken in the Fe I λ5576 and C I λ5380 lines to verify the results just discussed and to obtain information about the height dependence of the velocities in and around flux tubes. The nonmagnetic Fe I λ5576 line has the additional advantage of providing a "clean" velocity measurement. We note that the different spectral lines were not observed simultaneously. Figure 8 shows the Doppler velocity, the corresponding Fe I λ5576 wing intensity, and the G-band intensity, respectively. The spot is in the lower

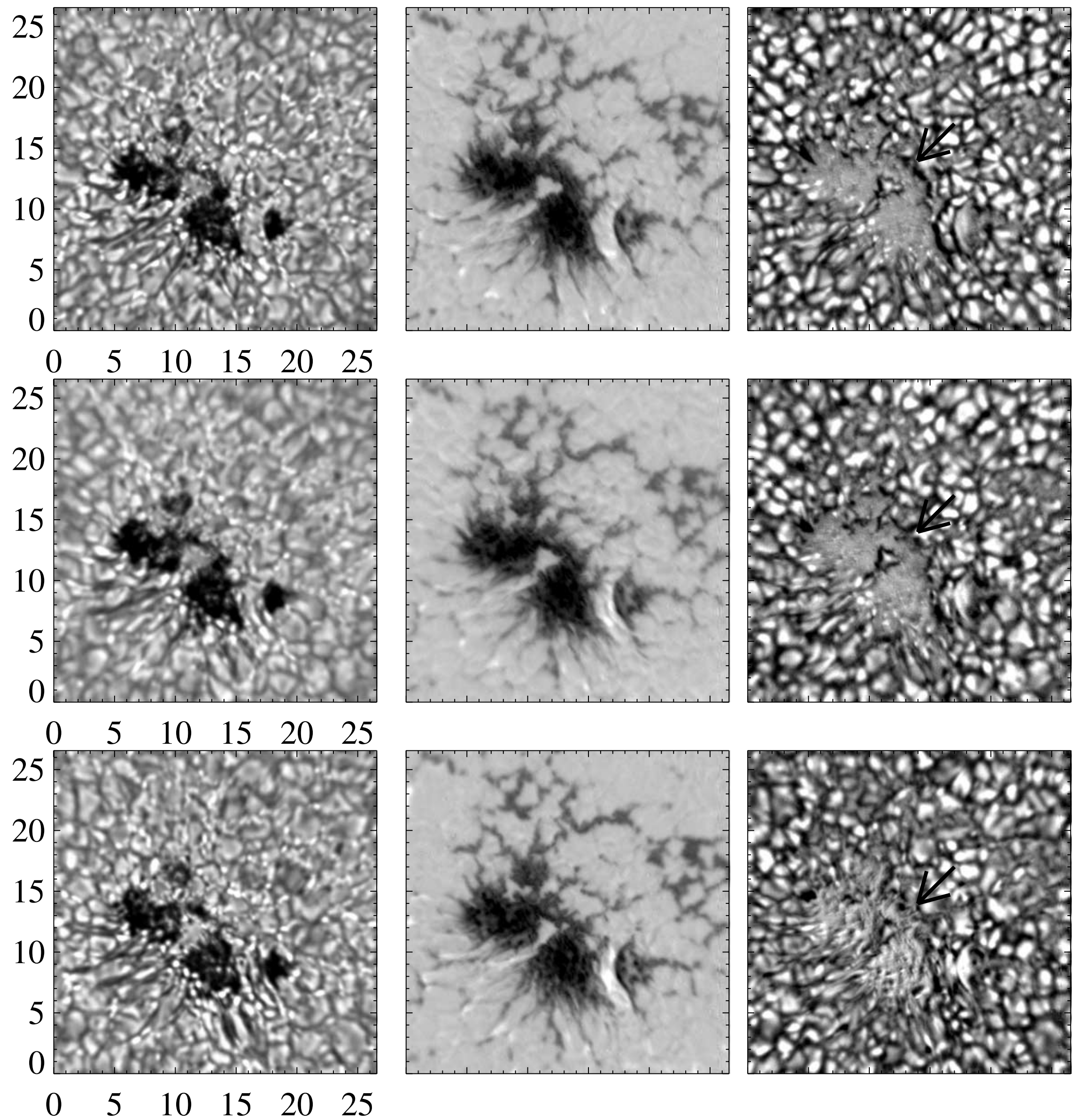

FIG. 3.—Time evolution of active region. Time progresses from bottom to top. Shown are G-band images (*left*), magnetograms (*middle*), and Dopplergrams (*right*) at three different times spanning a total of 45 minutes. Axis tick marks are in arcseconds. Strong downflows at the umbra-photosphere interface are marked with arrows.

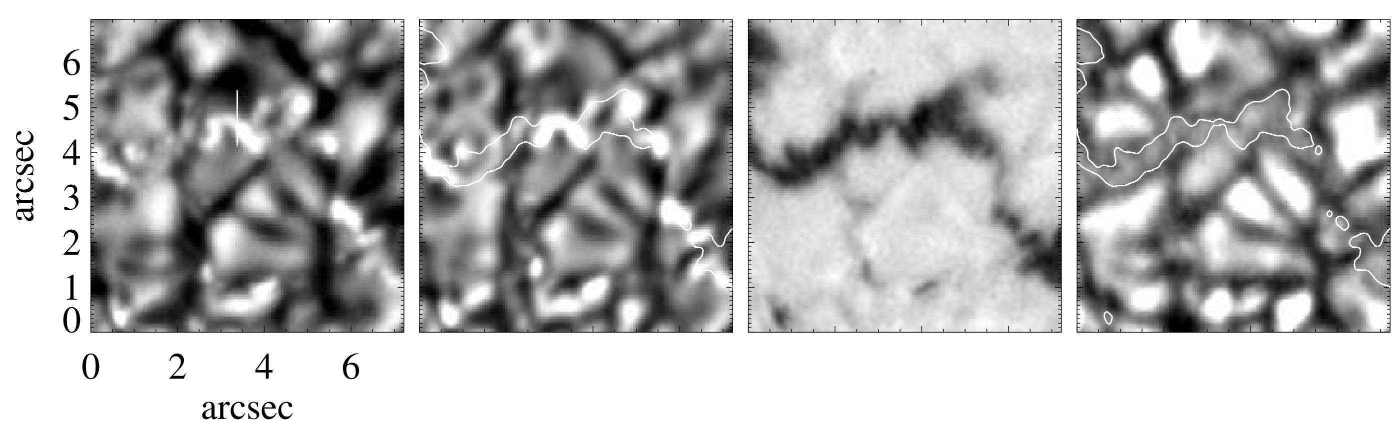

FIG. 4.—Close-up of BP region. From left to right: G-band intensity, Fe I λ6302 wing intensity, magnetogram, and Dopplergram. The contours outline the LOS magnetic field.

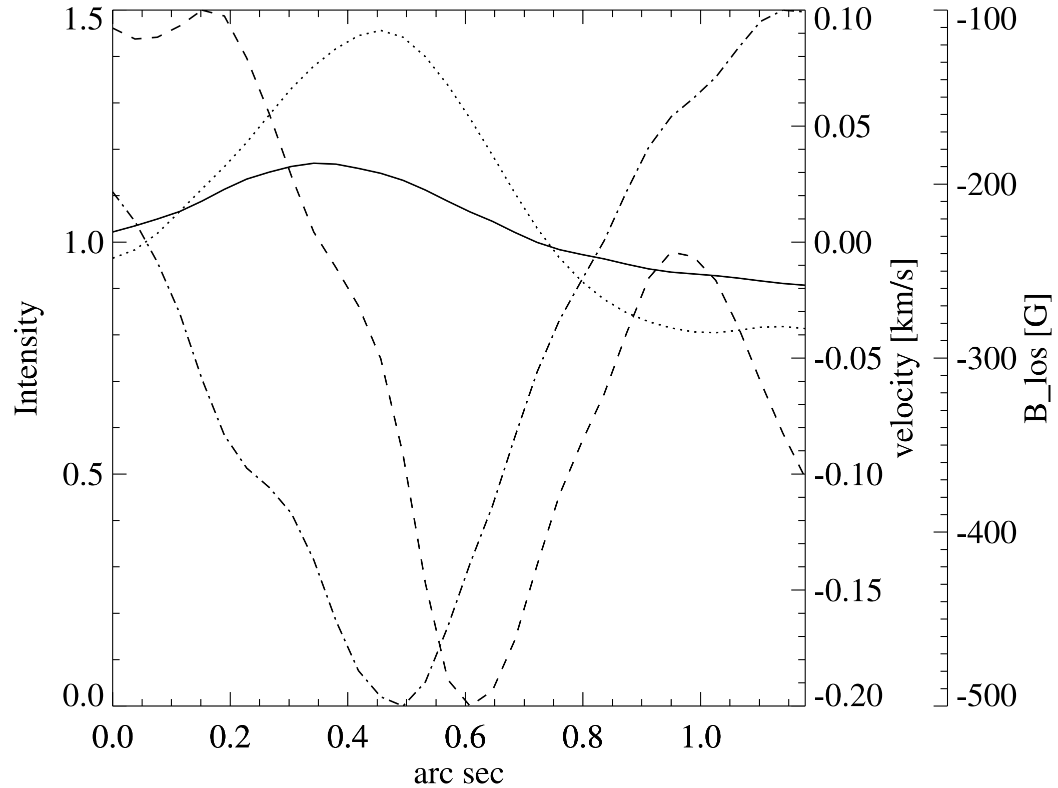

Fig. 5.—Cross section through an individual BP as marked in Fig. 4: G-band intensity (*dotted line*), Fe I λ6302 wing intensity (*solid line*), LOS component of the magnetic field (*dash-dotted line*), and velocity (*dashed line*). A downflow is observed at the edge of the magnetic flux concentration. Positive velocities denote downflow.

left corner of the approximately $9'' \times 9''$ FOV. We note that BPs often are colocated with very low amplitude velocities of similar small spatial scale. Near the edge of BPs we often find narrow and strong plumes of downflowing plasma. The small-scale, low-amplitude velocity pattern associated with the BP areas shows structure near the diffraction limit of the DST ($<0''.2$).

Since we do not have simultaneous magnetograms, selecting pixels corresponding to flux concentrations is not as straightforward as in the case of the Fe I λ6302 Dopplergrams. In order to produce comparable scatter plots for the Fe I λ5576 line, we simply selected BP areas manually, as explained in the caption of Figure 9. Figure 9 shows scatter plots of Fe I λ5576 velocity versus G-band intensity. We plot velocity versus intensity for both the selected BP areas and "normal" granulation. Since the granulation area was selected from the close vicinity of the sunspot, the specification "normal granulation" is probably not entirely correct, since the granular convection is modified by the presence of the magnetic field.

We again find a bimodal distribution; i.e., the granular and the BP distributions can be clearly separated in this plot. As expected, for granulation we find a very good correlation between line intensity and velocity (correlation coefficient [C] of 0.74). The BP distribution also shows a good correlation between velocity and intensity ($C = 0.47$). This plot is very similar to what was show in Figure 7. On average, the BP regions show small downflows (183 m s^{-1}), and the brightest BPs have velocities close to zero. Again, it is likely that the small average downflow is due to contamination from intergranular lanes caused by the seeing halo of the PSF. In general, the velocity amplitudes of the BP regions are significantly smaller than the granular velocities.

Figure 10 shows examples of BPs as seen in the deep-forming line C I λ5380. We again show the line intensity, the G-band intensity, and the Dopplergram. BPs are also visible in the C I λ5380 line intensity, although their contrast is much lower and their shape is somewhat different for some of the BPs. The C I λ5380 Dopplergram shows relatively large scale upflows on the scale of granules and very small scale downflow plumes located in the intergranular lanes. These plumes are seen in particular near the edge of BPs. The size of the plumes is again of the order of the diffraction limit of the DST. Within the BPs themselves, we find small but significant downflows of 200–500 m s^{-1}. The downflow plumes at the edge of the BPs reach downward velocities of up to 1 km s^{-1}. We again caution that mixing of information from inside and outside the flux concentration due to imperfect PSF correction, in particular at spatial scales near the diffraction limit, may lead us to overestimate the amplitudes of the downflow within the BP (and underestimate the amplitude of the downflow plumes at the edge of the BP). Comparing the signature of the BPs and their surroundings in Dopplergrams from different altitudes, we conclude that the downflows appear significantly narrower and faster at deeper layers.

4.1.2. *Expansion of Bright Points with Height*

Blinking C I λ5380 line intensity images and simultaneously recorded G-band images reveals that the BPs appear smaller in the line intensity images. C I λ5380 forms very close to the bottom of the photosphere and, given the broad bandpass of the UBF, therefore could be looked at as a "near-continuum" image. Figure 11 shows cross sections through a number of randomly selected BPs. Plotted are the C I λ5380 line intensity and the G-band intensity. BPs seen in C I λ5380

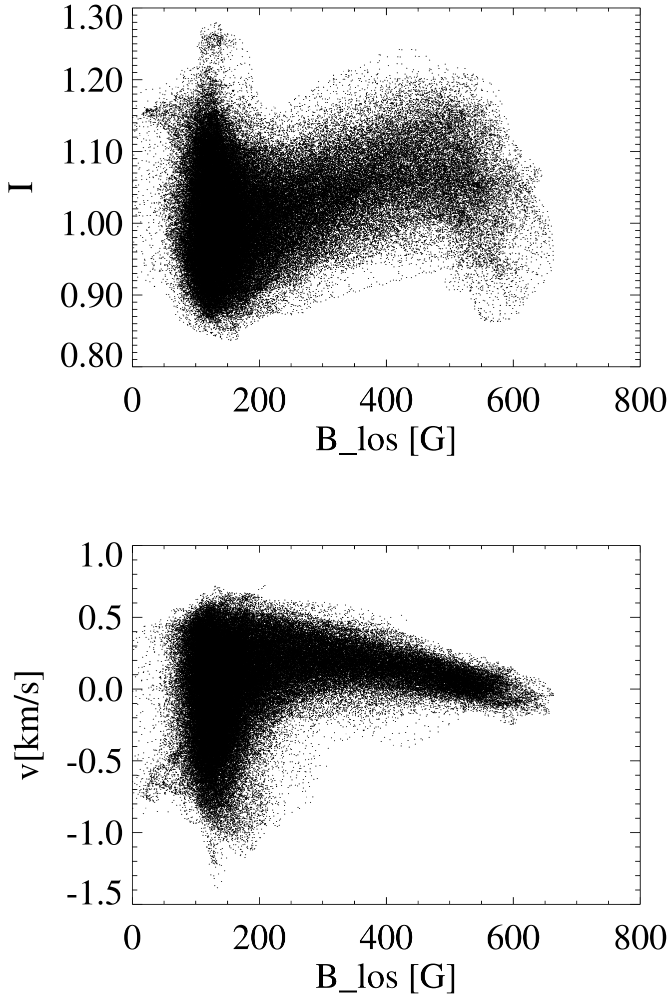

FIG. 6.—Scatter plot of B_{LOS} vs. intensity (*top*) and velocity (*bottom*) for magnetic flux concentrations. Positive velocity denotes downflow. In the range 200–500 G, we observe a linear increase of BP intensity with the measured flux density. For flux densities over 500 G, the features become dark, which we interpret as the onset of micropore formation.

are significantly brighter when observed in the G band. The contrast ratio is in the range of 1.2–1.5. We note that the absolute contrast values depend critically on how well we estimated the long-exposure PSF and should therefore be taken with some caution. Also given within each of the plots are the FWHMs of the line intensity and G-band profile. The apparent size of the BP is consistently and significantly smaller in the C I λ5380 intensity. The smallest C I λ5380 BP has an FWHM of 0\.17, which is very close to the diffraction limit of 0\.15 at 538 nm. The same BP has an FWHM of 0\.25 in the G band, where the diffraction limit is 0\.12 (430 nm). From Figure 11, we conclude that the apparent size of the BPs is between 30%–50% larger in the G band, as compared to the "continuum."

Figure 12 plots another set of examples of crosscuts through BPs, but in this case we plot the Fe I λ5576 intensity and compare to the G-band intensity. The apparent size of the BPs, as measured by their FWHM, is very similar in this case. The BPs tend to be just slightly smaller when observed in the Fe I λ5576 intensity. We note that these estimates of the apparent size of the BPs do not depend on the Strehl ratio being estimated correctly, as long as a diffraction-limited core is maintained in the PSF, which is clearly the case here. However, the diffraction-limited core could be broadened in the long-exposure PSF by residual tip/tilt errors. The fact that we observe structures very close to the diffraction limit of the telescope indicates that the broadening of the diffraction-limited core due to residual image motion is very small.

Figures 11 and 12 provide strong evidence for an expansion of the flux tubes (as observed by their intensity signature) as a function of height in the photosphere. Such an expansion is expected because of the rapid drop of gas pressure with height in the photosphere. Since the sizes of the observed BPs are very close to the diffraction limit, it is very difficult to estimate the real size of the BPs and compare their rate of expansion with height to model predictions. We also do not know the exact formation height of the observed features. We therefore cannot give any quantitative figures for how fast flux concentrations expand as a function of height. However, we can

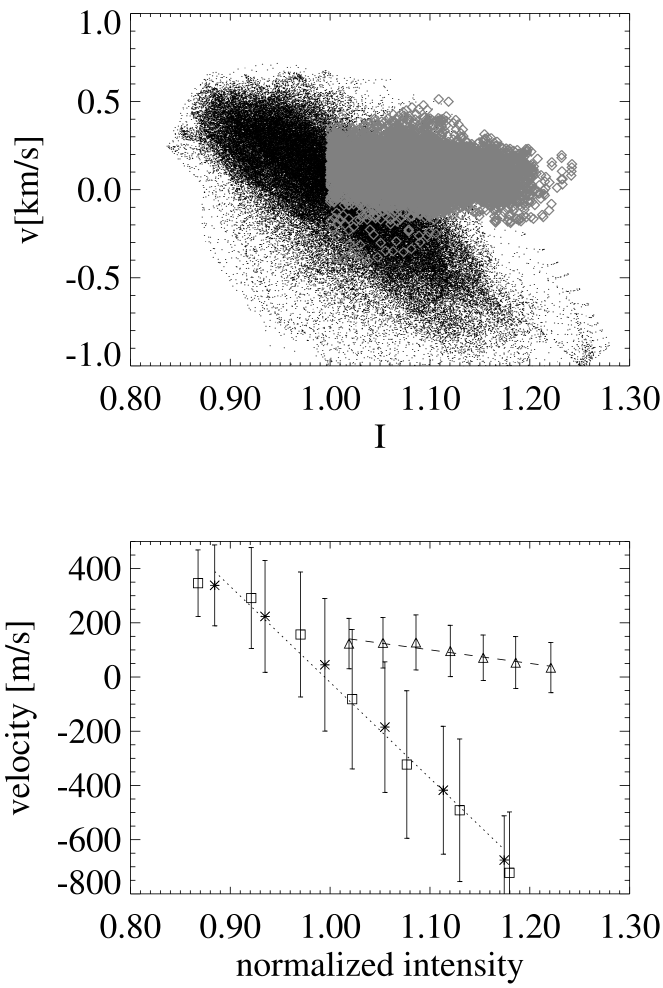

FIG. 7.—*Top*: Scatter plot of velocity vs. intensity for the same pixels that were selected for Fig. 6, but with $B_{\mathrm{LOS}} < 500$ G, i.e., excluding micropores. A bimodal distribution is visible. The gray diamonds represent the high-flux points in the range 300 G $< B_{\mathrm{LOS}} <$ 500 G and normalized intensity of more than 1. By applying these selection criteria, we select the interior of magnetic flux elements, i.e., BPs. The small black dots represent the low-flux points with $B_{\mathrm{LOS}} < 200$ G. These points represent the edges of magnetic elements. The velocities measured here are "contaminated" by the surrounding granular flow field. *Bottom*: Same as top panel, but data points were sorted into equidistant bins, and the average value was plotted with 1 σ error bars. The lines represent linear fits to the data points. *Asterisks*: Low-flux points; *squares*: quiet granulation for comparison; *diamonds*: high-flux points. The velocity of the brightest high-flux points (*triangles on dashed line*) approaches values close to zero.

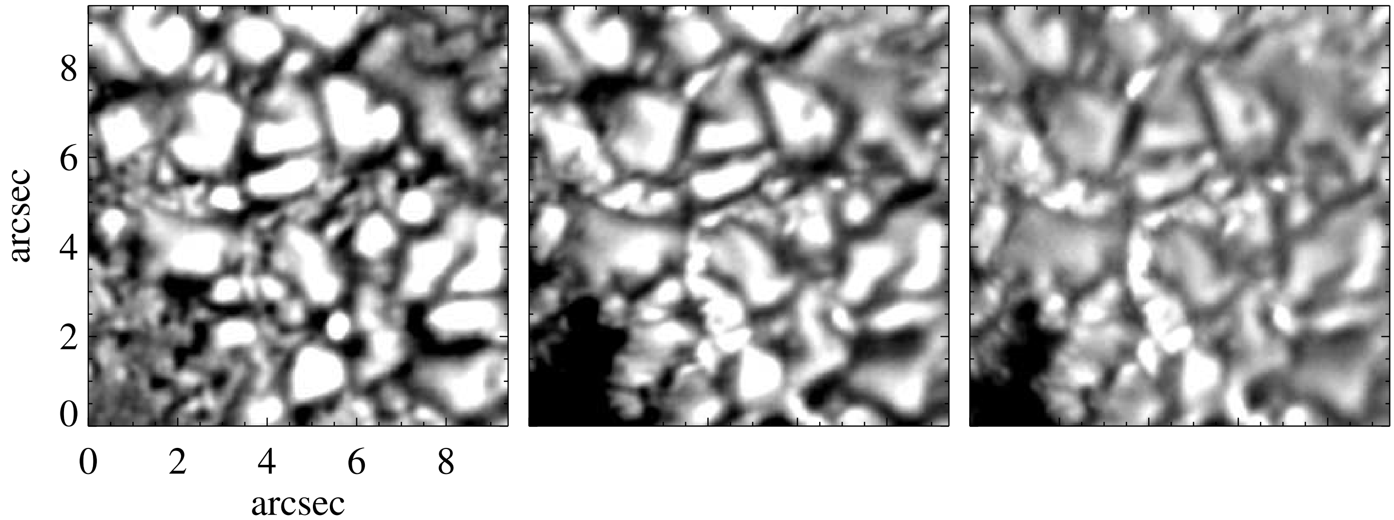

FIG. 8.—Close-up of BP region. Fe I $\lambda5576$ Doppler velocity (*left*), Fe I $\lambda5576$ wing intensity (*middle*), and G-band intensity (*right*). Effective exposure time: 30 s. Colocated with the BP regions we find a small-scale, low-amplitude velocity pattern. We find narrow downflow plumes (<500 m s^{-1}), colocated with small, dark features at the edges of BPs.

derive some rough bounds for the formation height of the G band. Figure 12 indicates that the G band forms at a height close to where the Fe I $\lambda5576$ line forms. According to Bruls et al. (1991), in a flux tube atmosphere the core of Fe I $\lambda5576$ forms at an altitude of 320 km. The UBF passband is broad compared to the width of the spectral lines observed. This means that a wide range of heights, including continuum, contribute to the UBF intensity images. Without detailed modeling, which is beyond the scope of this paper, we cannot derive an effective formation height for the UBF filtergrams. We can only state that the effective formation height is below the height where the Fe I $\lambda5576$ line core is formed.

From Figure 11, we conclude that the G-band formation height is well above the continuum, and Figure 12 indicates that the G band forms below 320 km (the core of Fe I). This height range is consistent with the calculations by Steiner et al.

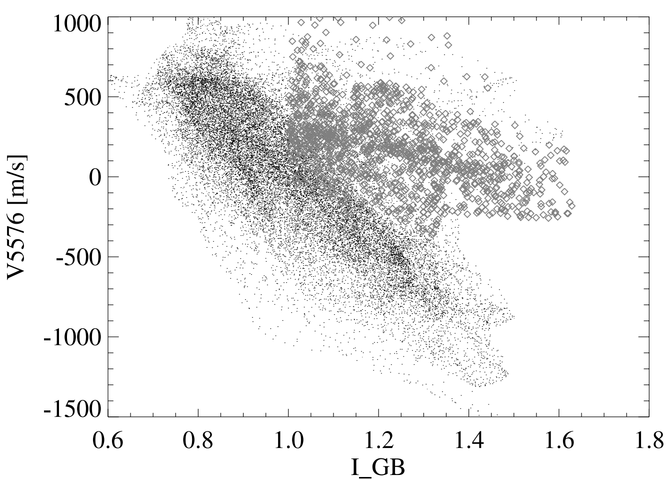

FIG. 9.—Scatter plot of Fe I $\lambda5576$ velocity vs. G-band intensity for BP areas (*diamonds*) and granulation (*dots*). The $g = 0$ Fe I $\lambda5576$ line is not subject to Zeeman splitting and therefore provides a clean velocity measurement. BP regions were selected using the cursor to trace along the boundaries of chains of BPs. As in the case of the velocities measured in Fe I $\lambda6302$ (Fig. 7), here the velocity of the brightest points also tends toward values close to zero.

(2001), who quote a formation height of 140 km for the core of the CH lines in the G band. On the other hand, Sánchez Almeida et al. (2001) argue for a G-band formation height very close to the visible continuum formation height, which is not consistent with our observations. Solanki et al. (1999) models the expansion of magnetic flux tubes and predicts an expansion of a few hundred kilometers over a height range of 300 km for small flux tubes. Keeping in mind the caveats mentioned above, Figure 11 seems to suggest a significantly slower expansion rate.

4.2. *Formation of Micropores*

Micropores are expected to form in intergranular lanes, in particular at vertices of intergranular lanes, where flux accumulates most efficiently (Stein et al. 2002). Once a sufficient amount of magnetic flux is accumulated, the micropore becomes dark with respect to the surroundings. This is because the $\tau = 1$ level of the partially evacuated magnetic flux concentration is depressed and cuts the micropore at a lower temperature than the surroundings. For small flux concentrations the opposite is true. The $\tau = 1$ level cuts the flux tube at a higher temperature than the surroundings, and the structure appears bright. Radiative heating of the edges of the flux tube, the hot-wall effect, contributes further to the brightening of the small flux tube. Figure 13 shows the evolution of flux concentrations, including several micropores, over a period of 12 minutes. Shown are G-band images and Fe I $\lambda6302$ Dopplergrams. In both cases, $B_{\rm LOS}$ contour lines were overplotted to outline the location of the magnetic field. In the first frame of the sequence, we observe a micropore beginning to form. Slight darkening occurs at several locations in the magnetic structure near the center of the FOV. Four minutes later (frame 2), two distinct micropores are visible. The same micropores are still visible in the last frame of the sequence, and they have become darker yet.

An interesting aspect of the evolution of the LOS magnetic field is the spatial distribution of the flux. At the beginning of the micropore formation, $B_{\rm LOS}$ shows a nearly symmetric distribution, as indicated by the contour lines. The second time step shows the maximum of $B_{\rm LOS}$ offset to one side and toward the edge of the dark micropore. The third time step

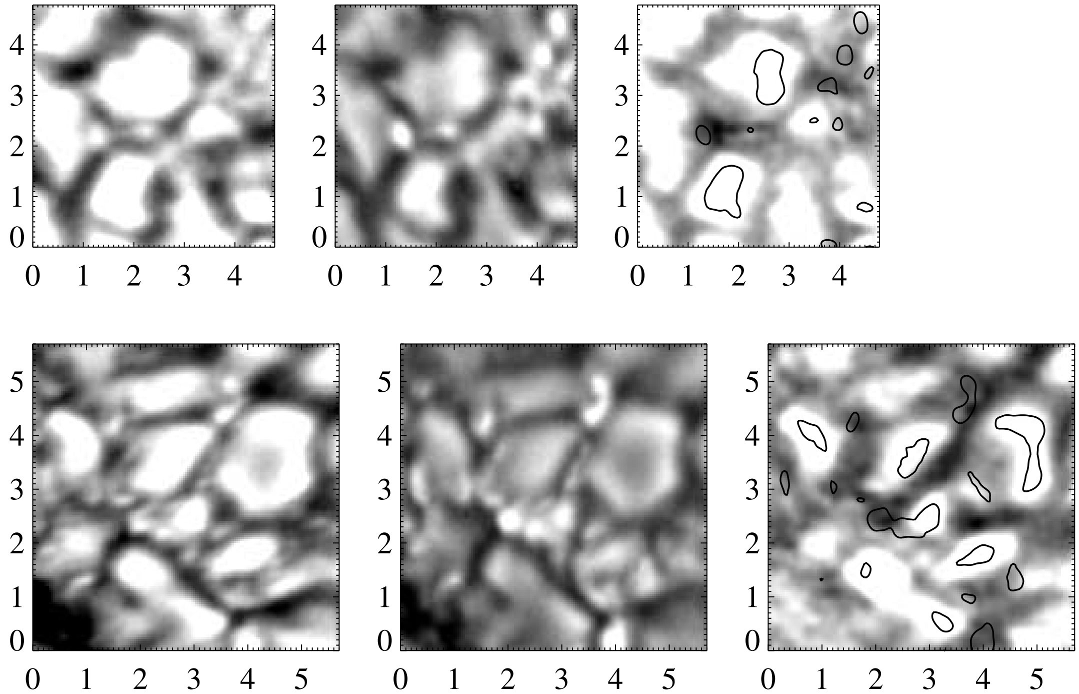

FIG. 10.—Close-up of selected BP regions. Effective exposure time: 30 s. *Left*: C I λ5380 intensity; *middle*: G-band intensity; *Right*: C I λ5380 velocity with G-band intensity contour lines overlaid. Units are arcseconds.

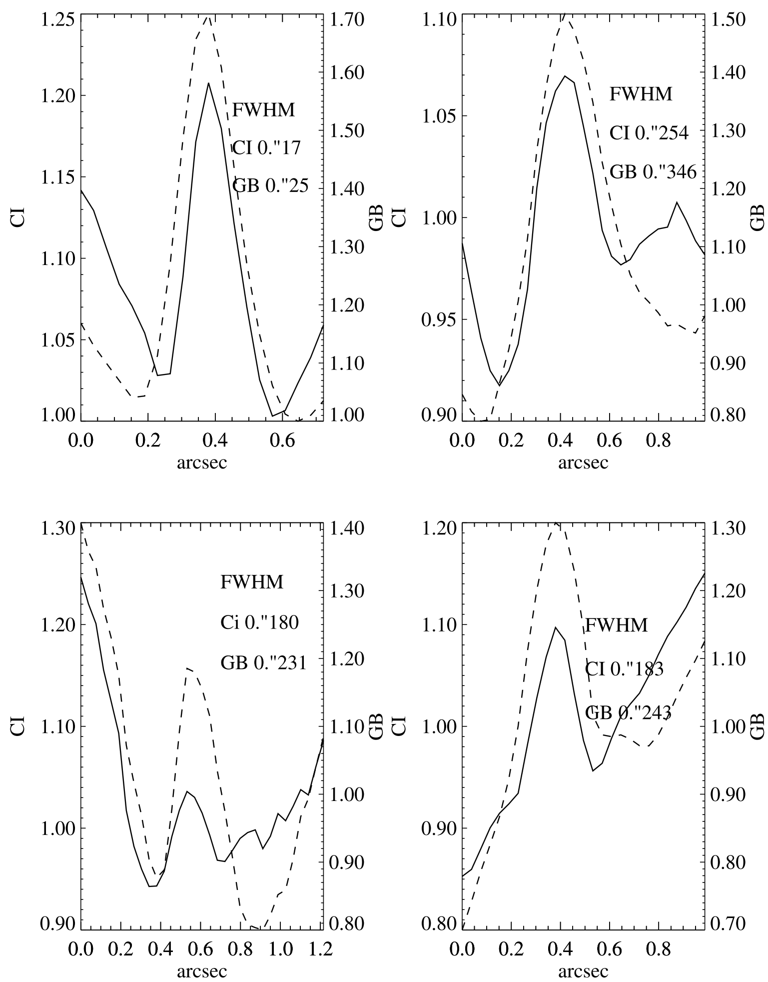

FIG. 11.—Cross sections through individual BPs: G-band (*dashed line*) and C I λ5380 intensity (*solid line*). The FWHM diameters are also given.

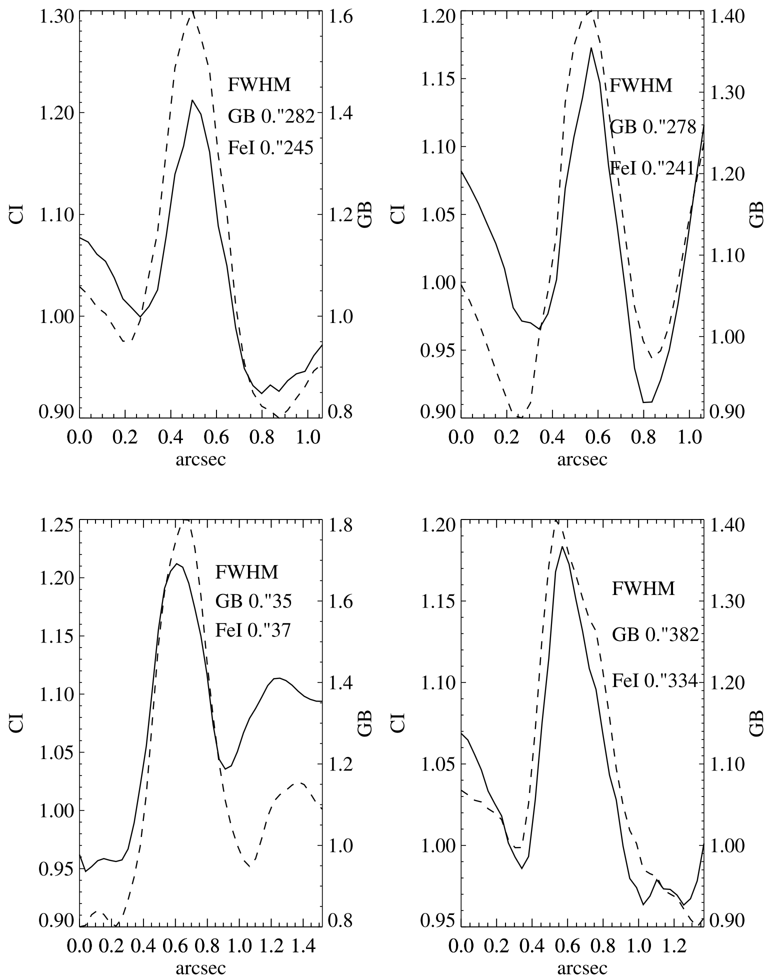

FIG. 12.—Same as Fig. 11, but comparing G-band and Fe I $\lambda5576$ intensity

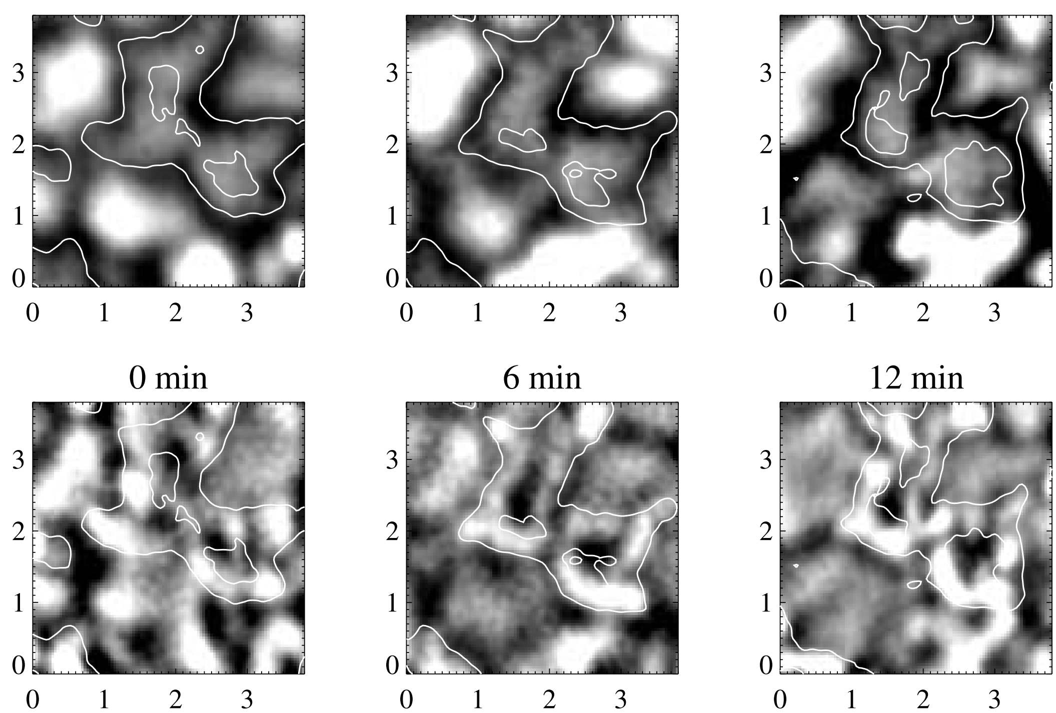

FIG. 13.—Formation of micropores. *Bottom*: G-band intensity, with LOS-magnetic field contours (300 and 600 G). *Top*: Velocity, with the same LOS-magnetic field contours. Units are arcseconds. See text for details.

again shows the maximum of $B_{\rm LOS}$ not centered on the dark micropores, although for the larger micropore the $B_{\rm LOS}$ maximum and intensity minimum are beginning to move closer together. Unfortunately, we do not have a long enough time sequence to study the formation and evolution of the micropore during all stages of its life. It is interesting to note that the MHD model calculations by Stein et al. (2002) predict such an arrangement, where in the early stages of micropore formation the intensity minimum is not colocated with the maximum of the magnetic flux. According to Stein et al. (2002), a granule is "squeezed out of existence as the magnetic field initially forms a ring around it." As the granule disappears, the flux concentrates at the intergranular lane vertex.

Figure 13 again demonstrates that the edges of these flux concentrations predominantly show downflows, whereas inside the flux tube the velocities are very small. In the first frame and at the location of the large micropore near the center of the FOV, we observe small-scale (0″.2) downflows in the Dopplergram. This substructure disappears as the micropore forms.

4.3. *Flows along the Magnetopause*

We observe narrow sheets of downflowing plasma near the edge of several magnetic features, indicating that these downflows seem to be a feature commonly found at the boundary of a strong magnetic field with its neighboring field-free plasma, i.e., at a magnetopause. In Figure 3, a narrow sheet of downflow can be seen at the edge of the umbra. The downflows are seen in both Fe I λ6302 and Fe I λ5576 Dopplergrams and in some cases persist over the entire observing period of 45 minutes. A particularly interesting example provides the bright area separating the two umbral fragments, which has many features in common with what is usually referred to as a strong LB. This indicates a similar physical origin of this structure, and we therefore also use term LB, recognizing that this particular LB does not entirely fit the criteria of this classification (Sobotka, Bonet, & Vázquez 1994; Rimmele 1997; Leka 1997).

Figure 14 shows a narrow ring of downflow outlining the edge of the LB. Close inspection reveals that the downflows occur at the edge of BPs arranged in a chain that outlines the boundary of the LB. This is especially apparent in Figure 14 (*right*), which shows the Fe I λ6302 Dopplergram, along with the LOS magnetogram and the G-band intensity. Intensity contour lines are added for easier orientation. The velocity amplitudes measured are in excess of 800 m s^{-1}. In the center of the LB, we observe upflows on the order of 500 m s^{-1}. The magnetogram reveals that the center area of the LB is nearly field-free. We note that the LB exhibits a significant polarization signal in the uncorrected magnetograms. This is due to the seeing halo of the PSF (width of $\approx 1''$) spreading the strong polarization signal originating in the umbra into the immediate surroundings.

We observe very similar narrow sheets of downflow in the Fe I λ5576 Dopplergram. We note again that the filtergrams for different wavelengths were taken several minutes apart. These downflows coincide with narrow dark lanes that are barely resolved in these data. These dark lanes are very likely similar to the narrow dark lanes observed by Scharmer et al. (2002), who dubbed these features "canals." Parts of the LB seen in the Fe I λ5576 filtergrams resemble the chainlike structures that are common for what is usually called a strong LB (see Sobotka et al. 1994 and references therein). In the center of LB, we find moderate upflows on a spatial scale of about $1''$. These upflows are more visible in the deep-forming carbon line. Narrow and localized plumes of downflows are seen in narrow dark lanes between these upflows. The impression is that the downflows become narrower and converge at deeper layers in the photosphere. Bright, pointlike structures show no velocity in C I λ5380 and Fe I λ6302, and they occasionally show slight upflows in the highest forming line, Fe I λ5576. The BPs form a ring outlining the bright region between the two major umbral fragments, similar to the bright ring often observed around a pore.

At the boundary of the field-free region and the umbral fragment, we observe a fluted structure of inclined magnetic field interlaced with nearly horizontal field (see Fig. 14, *middle right panel*). The BPs appear to form the footpoints of the highly inclined magnetic "filaments" very similar to the penumbral grains that form the footpoints of penumbral filaments (see § 4.4). Between the BPs are dark, elongated features of size 0″.2. The dark features coincide with a significantly smaller, but still measurable, LOS component of the magnetic field; i.e., the field appears more horizontal here. Vector field measurements with this or better resolution are needed to arrive at a definite picture of the three-dimensional field geometry.

Our observations suggest that these features are similar to the small-scale features recently observed at the 0.95 m New Swedish Solar Telescope that were dubbed "hair" by Scharmer et al. (2002). The fluted magnetic field structure at the magnetic-nonmagnetic interface (magnetopause) is similar to what is observed in the penumbra (e.g., Title et al. 1993; Martens et al. 1996; Neukirch & Martens 1998).

4.4. *Penumbral Filaments*

The active region observed had a rudimentary penumbra. As a result of the fact that the sunspot was located almost exactly at disk center, we were able to get a rare measurement of the vertical component of the flow field associated with penumbral filaments. Since the penumbra was not fully developed, we were able to identify and isolate what we believe are individual penumbral filaments, in order to study their flow pattern.

Figure 15 shows the G-band intensity, Fe I λ6302 intensity, magnetogram, and Dopplergram of the selected filaments. Two narrow (<0″.2), elongated structures are visible within the FOV. In particular, in the G-band image it becomes apparent that the dark filaments seem to originate in the "bright filament footpoint" in the inner penumbra (i.e., close to the umbral boundary). The same bright features are also visible in the Fe I λ6302 intensity but are less prominent there because of the lower resolution at this wavelength. Looking at the Doppler- and magnetograms, we find that colocated with the bright filament footpoint are strong upflows and a significant vertical field component. This is clearly seen in Figure 16, where we trace intensity, velocity, and $B_{\rm LOS}$ signals along one of the filaments. The bright filament footpoint has an FWHM of about 0″.2, and within this same distance the transition from bright filament footpoint to dark filament tail occurs. Since we are operating very close to the diffraction limit of the telescope the actual sizes and distances maybe even smaller. The bright filament footpoint is associated with an upflow of about 200 m s^{-1} and a strong LOS component of the field. As the filament turns dark, both the velocity and the $B_{\rm LOS}$ signals assume values consistent with zero. This observation would be consistent with a horizontal filament that continues to carry a flow along the filament axis. However, because the spot is right at disk center, the horizontal flow is not visible to us in the dark, horizontal part of the filament. These observations

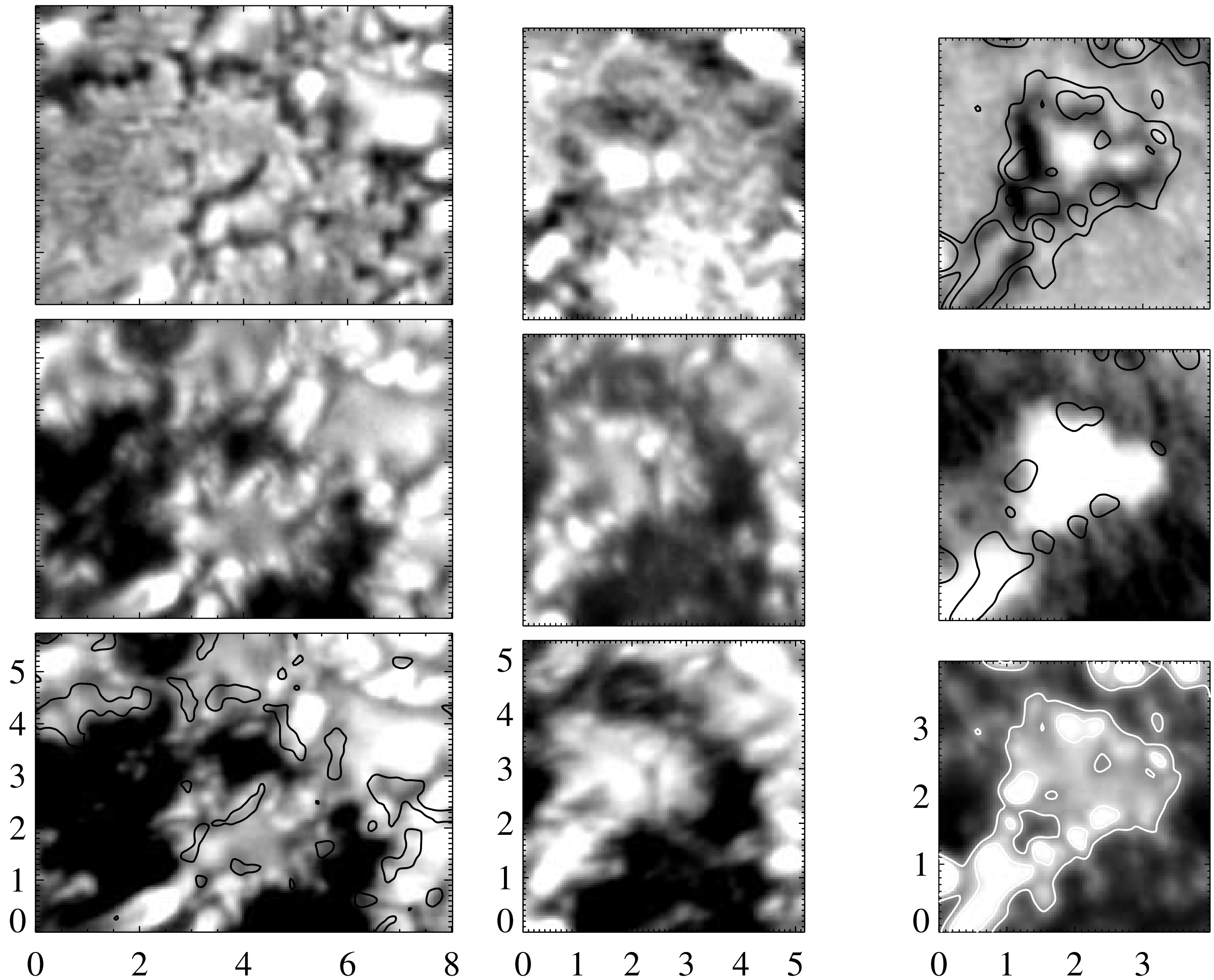

FIG. 14.—Close-up of the bright region seen between the two large umbral fragments (see Fig. 2). The magnetogram (*middle right*) indicates that this region is field-free. This feature could be interpreted as a large LB. *Left, top to bottom*: Fe I λ5576 velocity, G-band intensity, and Fe I λ5576 intensity. Contours of downflow velocities have been added to the intensity image. *Middle, top to bottom*: C I λ5380 velocity, G-band intensity, C I λ5380 intensity. *Right, top to bottom*: Fe I λ6302 velocity with intensity contours overlaid, Fe I λ6302 magnetogram, and Fe I λ6302 intensity. Intensity contours have been added for better orientation. Units are arcseconds.

suggest that the bright footpoint is an integral feature of penumbral filaments and that it may well be related to, or even the source of, the penumbral grains.

4.5. *Umbral Dots*

A number of umbral dots are seen within the umbral fragments of the observed active region. The size of the umbral dots is near the diffraction limit of the DST (0.″15 at 538 nm). Figure 17 displays intensity maps and Dopplergrams of one of the umbral fragments for the Fe I λ5576 line (upper photosphere) and the C I λ5380 line (lower photosphere). We note that the two wavelengths were observed about 20 minutes apart. The surprising result is that looking at the C I λ5380 Dopplergram, we find very strong upflows in excess of 1 km s^{-1} that are colocated with bright umbral dots. With the exception of areas close to the edge of the umbra, there is no indication of the existence of corresponding downflows of similar amplitude in which the upward-moving plasma might return back down. In contrast, the Fe I λ5576 Dopplergram does not show the strong upflows correlated with bright umbral dots. The velocities measured in Fe I λ5576 are of the order of less than $\pm$300 m s^{-1} only. This indicates that the umbra shows little sign of plasma motion at upper layers of the photosphere, while in the deeper layers represented by the C I λ5380 line, we observe signs of rigorous plasma motion, namely, upflows. Using the high-forming Fe I λ5576 and λ5434 lines, Wiehr (1994) finds no systematic Doppler shifts, nor are line asymmetries found in umbral dots with respect to their interdot neighborhood. Schmidt & Balthasar (1994), as well as Rimmele (1997), find no or only very small velocities in umbral dots when using lines that form in the mid-to-upper photosphere. This is consistent with our observations, since we only measure significant velocities in umbral dots in the deepest layers of the photosphere. Other studies (e.g., Kneer 1973; Pahlke & Wiehr 1990) report a significant upflow velocity of the order of a few kilometers per second and a significantly reduced field strength in umbral dots. We speculate that the discrepancy between different velocity measurements

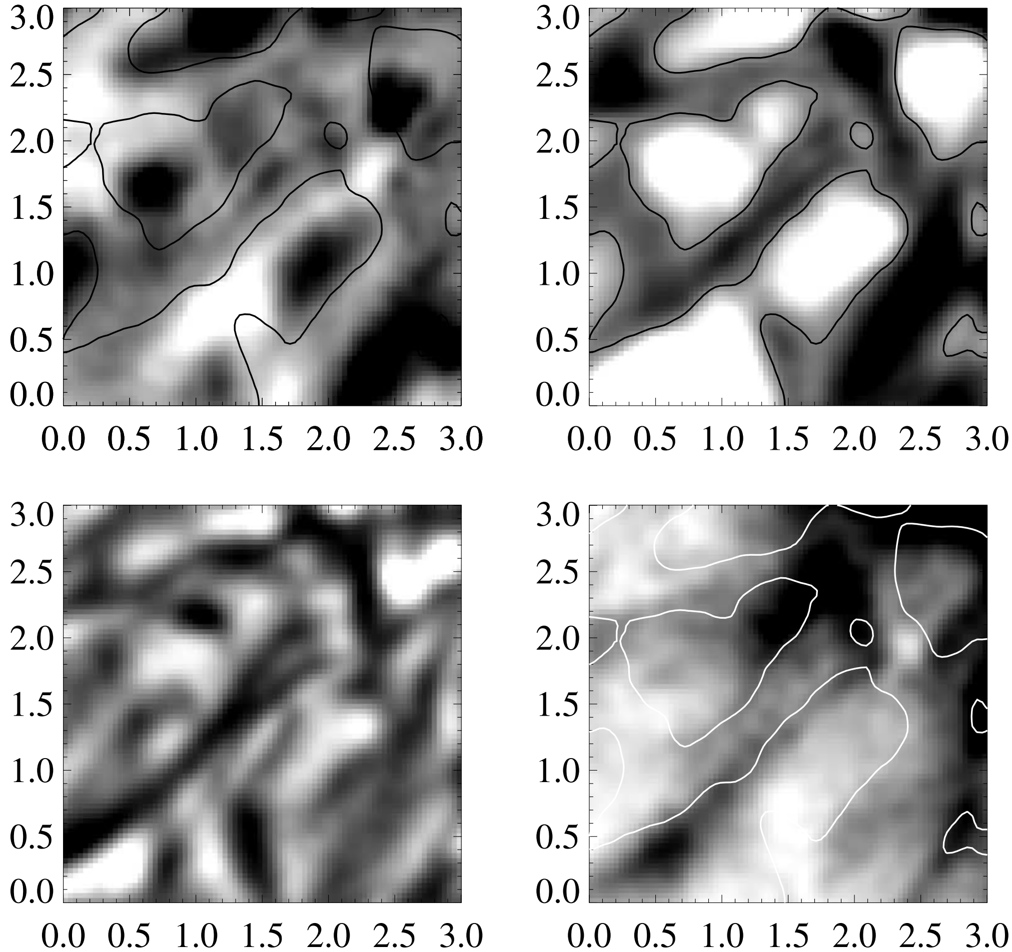

FIG. 15.—Close-up of individual penumbral filaments. *Bottom*: G-band intensity (*left*) and magnetogram (*right*). *Top*: Dopplergram (*left*) and Fe I λ6302 wing intensity (*right*). Units are arcseconds.

reported for umbral dots may be due to the fact that different spectral lines were used for the various studies. As is the case for our C I λ5380 observations, Kneer (1973) used a spectral line that forms close to the continuum level. Pahlke & Wiehr (1990) use a set of lines including deep-forming, weak lines.

5. SUMMARY

We used AO-corrected, diffraction-limited filtergram and imaging data to study small-scale magnetic features, including flux concentrations (flux tubes), seen in an active region at disk center. The AO allowed us to obtain long-exposure, narrowband imaging at the diffraction limit, from which Dopplergrams and magnetograms were computed. An attempt was made to correct for the effects of residual aberrations by modeling the long-exposure PSF of a partially correcting AO system. The results are summarized in the following subsections.

5.1. *Flux Concentrations and Bright Points*

1. Strong, narrow downflows are observed at the edge of many small ($<0''.2$) flux concentrations. In general, we do not find the rings of downflows around the flux tube, but rather downflow plumes at the edge of the flux concentration. The size of the downflowing areas is typically less than $0''.2$. The velocity amplitudes range from a few hundred meters per second to 1 km s^{-1}.

Narrow sheets of downflows are sometimes found at the edge of chains of BPs. These chains resemble the flux sheets modeled in two-dimensional MHD simulations, where slabs of downflows form at the edge of flux sheets. Apparently, the predictions of two-dimensional models should not be simply extrapolated to three dimensions by assuming that a slab becomes a ring when going to three dimensions. Since both the bright ring and downflows have the same physical origin (radiative losses into the tube). the hot-wall effect may therefore also not produce a bright ring, but rather small bright patches. Observations of even higher resolution and high-resolution (on the order of 10 km), three-dimensional MHD models are needed to make progress in this area.

2. Comparing the signature of the BPs and their surroundings in Dopplergrams from different altitudes, we conclude that the downflows appear significantly narrower and faster at deeper layers.

3. Within the flux concentration there is little plasma motion. The Dopplergrams recorded in the deep-forming C I λ5380 line show, on average, very small downflows of a few hundred meters per second. At higher layers in the photosphere, represented by the Fe I λ6302 and λ5576 ($g = 0$) Dopplergrams, and in the very center of the brightest flux concentrations, we observe velocities very close to zero; i.e., the plasma tends to be at rest in the center of flux concentrations.

In their simulations, Stein et al. (2002) find that considerable downward motions persist in small-scale flux concentrations,

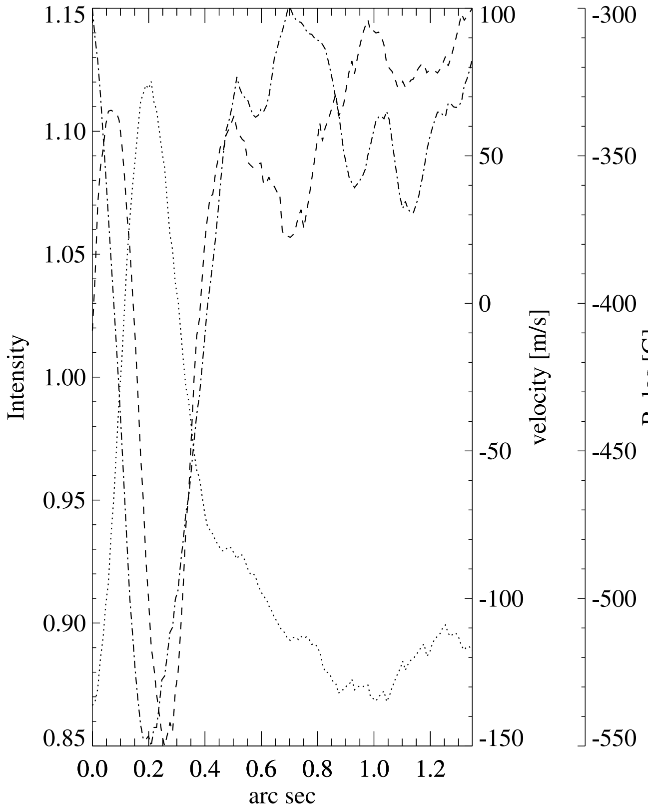

FIG. 16.—Trace along one of the penumbral filaments shown in Fig. 15: G-band intensity (*dotted line*), velocity (*dashed line*), and $B_{\rm LOS}$ (*dash-dotted line*).

whereas the material within micropores is at rest. The difference between our observations and the model prediction may be that in the simulation the early stages of flux tube formation, i.e., the evacuation process, is modeled, while we observe a set of mature flux tubes. A study of the dynamics of these downflow plumes is needed.

4. Flux concentrations with a flux density in the range 200–500 G show a linear increase of BP intensity with the measured flux density. For flux densities greater than 500 G the features become dark, which we interpret as the onset of micropore formation.

5. We find strong evidence for the expected expansion of magnetic flux concentrations with height. Even though we achieved the diffraction limit, the resolution is still insufficient to derive quantitative measurements of flux tube diameters as a function of height. Telescopes of aperture significantly larger than that of the DST are needed to provide such quantitative measurements.

5.2. *Micropores*

With a short time sequence of narrowband filtergrams and magnetograms, we observe the formation of micropores. During the early stages of micropore formation, the maximum of the (LOS) magnetic field is not centered on the dark micropores. This detail of the micropore formation process is consistent with model predictions (Stein et al. 2002)

5.3. *Plasma Flows along the Magnetopause*

We observe narrow sheets of downflowing plasma near the edge of several magnetic features, indicating that these downflows seem to be a feature commonly found at the boundary of a strong magnetic field with its neighboring field-free plasma, i.e., at a magnetopause. Besides downflows observed at the edge of small flux concentrations, we observe narrow sheets of downflow at the umbra-photosphere boundary and along the edge of an LB.

At the boundary between dark umbral fragments and the LB we observe chains of BPs. At the edge of these BPs we find strong, narrow downflows with amplitudes of several hundred meters per second. The width of what appears to be sheets of downflowing plasma is 0″.2 or less, i.e., at the diffraction limit of the DST. The downflows coincide with narrow dark lanes, which we believe are similar to the canals recently described by Scharmer et al. (2002). The narrow downflows, most likely driven by radiative losses into the evacuated magnetic structure, are fed by a large-scale (>1″) upflow in the center of the LB.

Furthermore, we observe a fluted structure of inclined magnetic field interlaced with nearly horizontal field. BPs appear to form the footpoints of the highly inclined magnetic "filaments," very similarly to the penumbral grains that form the footpoints of penumbral filaments. Between the BPs we see dark, elongated features of size 0″.2. The dark features coincide with a significantly smaller LOS component of the magnetic field, which we associate with a more horizontal field vector. The fluted magnetic field structure at the magnetic-nonmagnetic interface (magnetopause) is similar to what is observed in the penumbra.

5.4. *Penumbral Filaments*

We were able to identify and isolate what we believe are individual penumbral filaments, in order to study the vertical component of their flow pattern. Our observations suggest that a bright footpoint of size 0″.2 or less is an integral feature of penumbral filaments and that this BP may be related to, or even the source of, the penumbral grains. Colocated with the bright filament footpoint are upflows of the order of 200 m s^{-1} and a significant vertical field component. The transition from bright filament footpoint to dark filament tail occurs within a distance of less than 0″.2. As the filament turn dark, both the velocity and $B_{\rm LOS}$ signals assume values consistent with zero. This observation would be consistent with a horizontal filament that continues to carry a flow along the filament axis.

Our observations seem to confirm at least some specific aspects of the model by Schlichenmaier, Jahn, & Schmidt (1998). The model predicts a bright, nearly vertical filament footpoint that contains upflowing plasma, and the quick turnover into a horizontal filament would be consistent with the model. However, several discrepancies and open questions remain.

Our observational results are also interesting in the context of theoretical models. Schlichenmaier et al. (1998) model the dynamic evolution of a thin flux tube inside the penumbra. A flow develops along the flux tube as the tube rises through the thick penumbra. The flow, which the authors associate with the Evershed flow, is driven by local pressure differences. The model by Schlichenmaier et al. differs from the well-established siphon flow model (see Montesinos & Thomas 1997), in the sense that Schlichenmaier et al. apply an open boundary condition at the outer end of the penumbral flux tube. The model predicts (see Fig. 8 of Schlichenmaier et al. 1998) a filament structure that is characterized by a hot, nearly vertical upflow of plasma at the footpoint of the filament, which within a few hundred kilometers turns into a horizontal filament that is elevated by about 100 km above the surface.

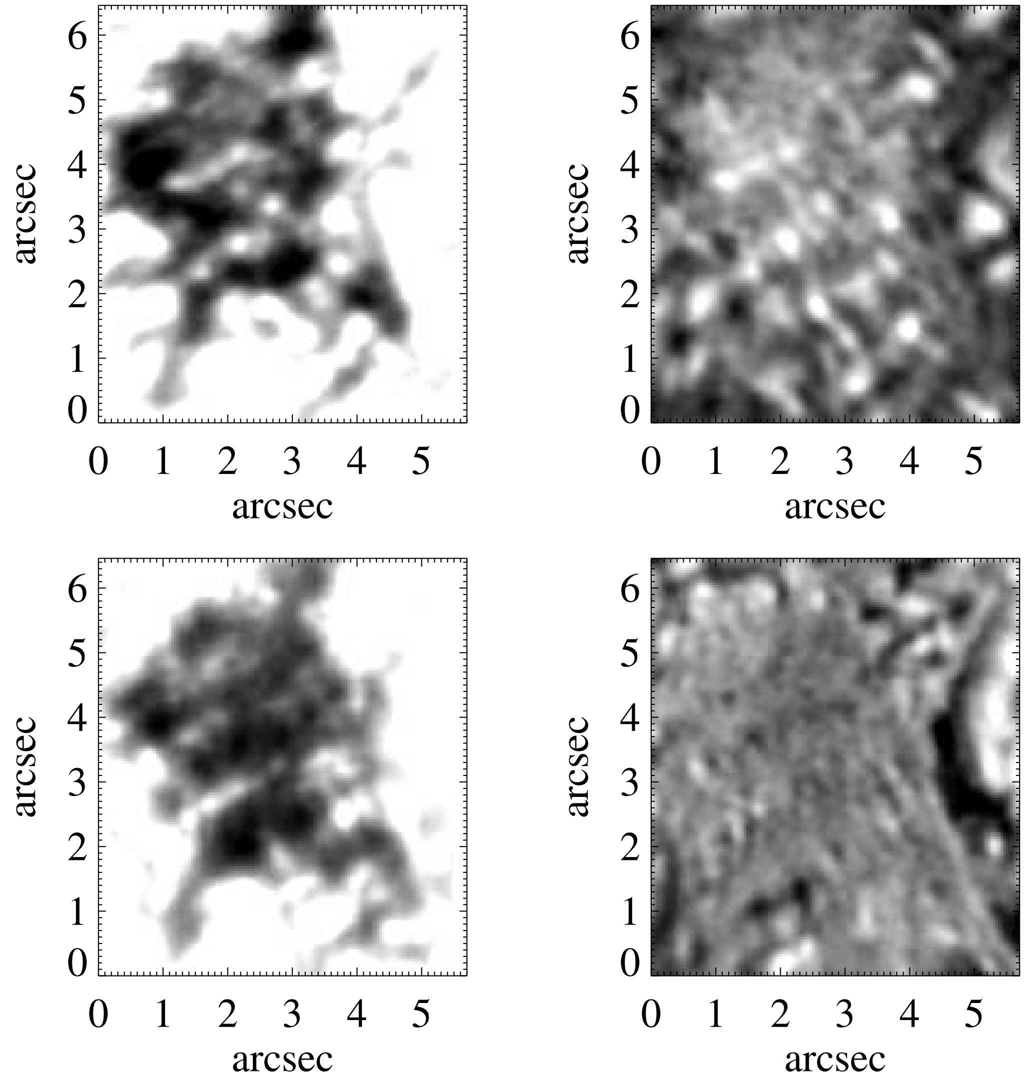

FIG. 17.—Umbral dots observed at two heights in the photosphere. *Bottom*: Fe I λ5576 wing intensity (*left*) and velocity (*right*). *Top*: C I λ5380 wing intensity (*left*) and velocity (*right*). In the C I λ5380 data, strong upflows in excess of 1 km s^{-1} are observed in umbral dots.

Schlichenmaier et al. discuss observational consequences of their model. At the footpoint the tube's temperature is higher than the corresponding background values, and the footpoint appears bright. They point out that the footpoint of the flux tube inside the penumbra could therefore be identified with a bright penumbral grain. As the plasma flows along the tube, it loses energy by radiation and cools off, and the filament becomes as dark as its surroundings.

Our observations seem to confirm at least some aspects of the Schlichenmaier et al. (1998) model. The bright, nearly vertical filament footpoint that contains upflowing plasma and the quick turnover into a horizontal filament would be consistent with the model. However, there are also several discrepancies and open questions. According to the model, the upflow should be of the order of 6 km s^{-1}, which is an order of magnitude more than what we observe. Previous observations have also shown upflows of a few hundred meters per second in bright penumbral grains (e.g., Rimmele 1995), which is consistent with the upflows we observe at the filament footpoint. Possible explanations for this discrepancy include insufficient resolution and the low excitation potential of the line used (Fe I λ6302), as explained by Schlichenmaier et al. (1998). We also note that the transition from bright footpoint to dark filament (with respect to the surroundings) occurs within 0$''$.2 (150 km), whereas in the model this transition occurs over many arcseconds. This might indicate that the plasma in the tube cools off much faster than the model predicts. Furthermore, the filaments do not appear to be embedded in a dark penumbral background; i.e., we do not see any evidence for the dark background component that, according to Schlichenmaier et al. (1998), carries an Evershed flow. Our observations show that the filaments are surrounded by granular convection instead. This also raises the question of what the role of the background field is in the formation of penumbral filaments, as well as the Evershed flow.

5.5. *Umbral Dots*

We observe umbral dots with size of the order of 0$''$.2. In the deepest layers of the photosphere we measure upflows in excess of 1 km s^{-1} in umbral dots, whereas in higher layers we find only small velocity amplitudes.

Knowing the physical processes responsible for the fine structure of a sunspot is crucial for understanding the subphotospheric structure of sunspots. Solanki (2003) provides a comprehensive review of sunspots, including sunspot models and sunspot fine structure. In the monolithic flux tube model, umbral dots are interpreted as the manifestation of overstable convection in a magnetic plasma (Knobloch & Weiss 1984; Weiss et al. 1990). According to the cluster model, a sunspot is a loose cluster of flux tubes that retain their individual identity during the lifetime of the sunspot. Below the surface, the individual flux tubes are separated by convecting, field-free gas. In this model, umbral dots are interpreted as the thermal signature of field-free gas that is pushing magnetic field lines aside and penetrating from below into the photosphere (magnetic valve; Parker 1979; Choudhuri 1986). The amplitude of the upflow is estimated to be of the order of several kilometers per second in the magnetic valve model (Choudhuri 1986). Knobloch & Weiss (1984) estimate upflow velocities of the order of 100 m s^{-1} for umbral dots. Our observations appear to be consistent with the cluster model for sunspots in this regard. However, additional observational data, such as magnetic field strength measurements in umbral dots, are needed before we can distinguish conclusively between the two models.

I am grateful for the competent support received from the technical and observing staff at the DST. Many thanks to Kit Richards for ensuring that the AO system was operating to its full potential. I am grateful to Matt Penn for reading the manuscript and for providing valuable comments. Part of this work was supported by the National Science Foundation under grant 0079482.

REFERENCES

Bercik, D. J., Nordlund, Å., & Stein, R. F. 2003, in Local and Global Helioseismology: The Present and Future, ed. H. Sawaya-Lacoste (ESA SP-517; Noordwijk: ESA), 201
Berger, T. E., Löfdahl, M. G., Shine, R. A., & Title, A. M. 1998, ApJ, 506, 439
Berger, T. E., Schrijver, C. J., Shine, R. A., Tarbell, T. D., Title, A. M., & Sharmer, G. 1995, ApJ, 454, 531
Berger, T. E., & Title, A. M. 1996, ApJ, 463, 365
———. 2001, ApJ, 553, 449
Bruls, J. H. M. J., Lites, B. W., & Murphy, G. A. 1991, in Proc. 11th NSO Solar Polarimetry Workshop, ed. L. J. November (Sunspot: NSO), 444
Choudhuri, A. R. 1986, ApJ, 302, 809
Fleck, B. 1991, Ph.D. thesis, Univ. Würzburg
Gerrard, C. L., Arber, T. D., & Hood, A. W. 2002, A&A, 387, 687
Grossmann-Doerth, U., Schüssler, M., Sigwarth, M., & Steiner, O. 2000, A&A, 357, 351
Grossmann-Doerth. U., Schüssler, M., & Steiner, O. 1998, A&A, 337, 928
Hartkorn, K. 2003, Ph.D. thesis, New Jersey Inst. Technology
Kneer, F. 1973, Sol. Phys., 28, 361
Knobloch, E., & Weiss, N. O. 1984, MNRAS, 207, 203
Leka, K. D. 1997, ApJ, 484, 900
Leka, K. D., & Steiner, O. 2001, ApJ, 552, 354
Martens, P. C. H., Hurlburt, N. E., Title, A. M., & Acton, L. W. 1996, ApJ, 463, 372
Montesinos, B., & Thomas, J. H. 1997, Nature, 390, 485
Muller, R. 1975, Sol. Phys., 45, 105
———. 1994, in Solar Surface Magnetism, ed. R. J. Rutten & C. J. Schrijver (NATO ASI Ser. C. 433; Dordrecht: Kluwer), 55
Muller, R., Dollfus, A., Montagne, M., Moity, J., & Vigneau, J. 2000, A&A, 359, 373
Muller, R., Roudier, Th., Vigneau, J., & Auffret, H. 1994, A&A, 283, 232
Neukirch, T., & Martens, P. C. H. 1998, A&A, 332, 1075
Nisenson, P., van Ballegooijen, A. A., de Wijn, A. G., & Sütterlin, P. 2003, ApJ, 587, 458
Pahlke, K.-D., & Wiehr, E. 1990, A&A, 228, 246
Parker, E. N. 1975, Sol. Phys., 40, 291
———. 1978, ApJ, 221, 368
———. 1979, ApJ, 234, 333
Piddington, J. H. 1975, Ap&SS, 34, 347
Rimmele, T. R. 1995, A&A, 298, 260
———. 1997, ApJ, 490, 458
———. 2000, Proc. SPIE, 4007, 218
Rutten, R., Kiselman D., Rouppe van der Voort, L., & Plez, B. 2001, in ASP Conf. Ser. 236, Advanced Solar Polarimetry: Theory, Observation and Instrumentation, ed. M. Sigwarth (San Francisco: ASP), 445
Sánchez Almeida, J., Asensio Ramos, A., Trujillo Bueno, J., & Cernicharo, J. 2001, ApJ, 555, 978
Sankarasubramanian, K., & Rimmele, T. 2002, ApJ, 576, 1048
Scharmer, G. B., Gudiksen, B. V., Kiselman, D., Löfdahl, M. G., & Rouppe van der Voort, L. H. M. 2002, Nature, 420, 151
Schlichenmaier, R., Jahn, K., & Schmidt, H. U. 1998, A&A, 337, 897
Schmidt, W., & Balthasar, H. 1994, A&A, 283, 241
Schüssler, M. 2001, in ASP Conf. Ser. 236, Advanced Solar Polarimetry: Theory, Observation and Instrumentation, ed. M. Sigwarth (San Francisco: ASP), 343
Schüssler, M., Shelyag, S., Berdyugina, S., Vögler, A., & Solanki, S. K. 2003, ApJ, 597, L173
Sigwarth, M., Balasubramaniam, K. S., Knölker, M., & Schmidt, W. 1999, A&A, 349, 941
Sobotka, M., Bonet, J. A., & Vázquez, M. 1994, ApJ, 426, 404
Solanki, S. K. 1993, Space Sci. Rev., 63, 1
———. 2003, A&A Rev., 11, 153
Solanki, S. K., Finsterle, W., Rüedi, I., & Livingston, W. 1999, A&A, 347, L27
Spruit, H. C. 1979, Sol. Phys., 61, 363
Stein, R. F., Bercik, D., & Nordlund, Å. 2002, Nuovo Cimento C, 25, 513
———. 2003, in ASP Conf. Ser. 286, Current Theoretical Models and Future High Resolution Solar Observations: Preparing for ATST, ed. A. A. Pevtsov & H. Uitenbroek (San Francisco: ASP), 121
Stein, R., Brandenburg, A., & Nordlund, Å. 1992, in ASP Conf. Ser. 26, Seventh Cambridge Workshop on Cool Stars, Stellar Systems and the Sun, ed. M. S. Giampapa & J. A. Bookbinder (San Francisco: ASP), 148
Stein, R. F., & Nordlund, Å. 1998, ApJ, 499, 914
Steiner, O. 1994, in IAU Symp. 154, Infrared Solar Physics, ed. D. M. Rabin, J. T. Jefferies, & C. Lindsey (Dordrecht: Kluwer), 407
———. 1999, in ASP Conf. Ser. 183, High Resolution Solar Physics: Theory, Observations and Techniques, ed. T. R. Rimmele, K. S. Balasubramaniam, & R. R. Radick (San Francisco: ASP), 17
Steiner, O., Grossmann-Doerth, U., Knölker, M., & Schüssler, M. 1998, ApJ, 495, 468
Steiner, O., Grossmann-Doerth, U., Schüssler, M., & Knölker, M. 1996, Sol. Phys., 164, 223
Steiner, O., Hauschildt, P. H., & Bruls, J. 2001, A&A, 372, L13
Title, A. M., & Berger, T. E. 1996, ApJ, 463, 797
Title, A. M., Frank, Z. A., Shine, R. A., Tarbell, T. D., Topka, K. P., Scharmer, G., & Schmidt, W. 1993, ApJ, 403, 780
van Ballegooijen, A. A., Nisenson, P., Noyes, R. W., Löfdahl, M. G., Stein, R. F., Nordlund, Å., & Krishnakumar, V. 1998, ApJ, 509, 435
Weiss, N. O., Brownjohn, D. P., Hurlburt, N. E., & Proctor, M. R. E. 1990, MNRAS, 245, 434
Wiehr, E. 1994, A&A, 287, L1